Time course of alterations in adult spinal motoneuron properties in the SOD1(G93A) mouse model of ALS

Seoan Huh[1], Charles J. Heckman[1,2,3], and Marin Manuel[1,4,§]

[1]Department of Physiology, [2]Department of Physical Medicine and Rehabilitation, and [3]Department of Physical Therapy and Human Movement Science, Northwestern University, Feinberg School of Medicine, Chicago, Illinois, USA. [4]Université de Paris, SPPIN - Saints-Pères Paris Institute for the Neurosciences, CNRS, Paris, France.

§ Corresponding author:

Marin MANUEL
SPPIN - Saints-Pères Paris Institute for the Neurosciences
Université de Paris, 45, rue des Saints-Pères, 75006 Paris, France
email: marin.manuel@neurobio.org

Author contribution

Conceptualization: S.H., C.J.H., and M.M.; Methodology: S.H., C.J.H., and M.M.; Investigation: S.H.; Formal analysis: S.H. and M.M.; Software: M.M.; Visualization: S.H. and M.M.; Writing - Original Draft: S.H.; Writing - Review & Editing: S.H., C.J.H., and M.M.; S.H., C.J.H., and M.M. approved final version of manuscript.

Number of pages: 33

Number of figures: 7 + 1 table

Number of words for abstract: 149

Number of words for Introduction: 514

Number of words for Discussion: 1860

Conflict of Interest

The authors have no conflict of interest to declare

Acknowledgements

This work was supported by NIH NINDS RO1NS077863 and NINDS RO1NS110953. S.H. was supported by a National Science Foundation Graduate Research Fellowship (NSF GRFP).

Abstract

Although ALS is an adult-onset neurodegenerative disease, motoneuron electrical properties are already altered during embryonic development. Motoneurons must therefore exhibit remarkable capacity for homeostatic regulation to maintain a normal motor output for most of the life of the patient. In the present paper, we demonstrate how maintaining homeostasis could come at a very high cost. We studied the excitability of spinal motoneurons from young adult SOD1(G93A) mice to end-stage. Initially homeostasis is highly successful in maintaining their overall excitability. This initial success, however, is achieved by pushing some cells far above the normal range of passive and active conductances. As the disease progresses, both passive and active conductances shrink below normal values in the surviving cells. This shrinkage may thus promote survival, implying the previously large values contribute to degeneration. These results support the hypothesis that motoneuronal homeostasis may be "hyper-vigilant" in ALS, and a source of accumulating stress.

Introduction

ALS is a fatal neurodegenerative disorder characterized by progressive loss of cortical and spinal motoneurons. Five to ten percent of the ALS cases are familial (FALS), and ～20% of the FALS cases are due to mutations in the Superoxide Dismutase1 (SOD1) gene (Rosen et al., 1993). Studies in the mutant SOD1 (mSOD1) mouse and other animal models have revealed that multiple cellular functions become impaired as the disease progresses (Ilieva et al., 2009; Kanning et al., 2009;

Johnson and Heckman, 2010; Brownstone and Lancelin, 2018), implying that homeostatic mechanisms are failing. Yet, the intrinsic excitability of neonatal and young adult mSOD1 motoneurons undergoes a very potent and effective homeostatic response to compensate an earlier surge in excitability in the embryonic state (Kuo et al., 2004; van Zundert et al., 2008; Pieri et al., 2009; Martin et al., 2013). The mechanisms of this successful homeostasis are however highly unusual.

The standard measure of the net excitability of motoneurons is the relation between frequency of firing of spikes and amplitude of injected current. This frequency-current (F-I) function is determined by multiple ionic currents. Remarkably, the successful F-I homeostasis in the neonatal state is achieved by abnormal but compensatory increases in these currents. Persistent inward currents (PICs), which are mediated by voltage gated Na^+ and Ca^{2+} channels, become aberrantly large. On its own, this change would increase F-I gain, but it is compensated by large increases in the leak currents that set the input conductance of the cell. These abnormal changes show that F-I homeostasis during the neonatal period is achieved via a compensatory mechanism. If, however, these compensatory increases persist into the young adult state, then the continued distortions in input conductances and PIC amplitudes could induce substantial stresses within the motoneurons. In this scenario, the initial success in homeostatic regulation of net excitability would be coupled to a severe cost, likely accelerating the onset of degeneration. On the other hand, if homeostatic processes instead successfully return input conductance and PIC values to normal ranges before the onset of

denervation, then homeostasis for the F-I function would reduce stress on the cell and effects on subsequent degeneration would likely be small.

To investigate how homeostasis for excitability develops as the disease progresses, we undertook the first *in vivo* voltage clamp studies of motoneurons in the mouse and pursued these measurements across a wide range of ages, from P30 to P120. This age range spans the young adult period, the onset of denervation period (∼P50, Pun et al., 2006) and the development of overt symptoms (∼P90). We hypothesized that input conductance and PIC values would continue to grow in the young adult state. Our results supported this hypothesis, revealing in fact a continual increase in amplitude of these parameters, followed by a collapse, so that motoneurons surviving beyond onset of overt symptoms (∼P90) had aberrantly small values of each. These results are consistent with the possibility that homeostasis for excitability is not in fact weak but excessively strong and that this overreaction contributes to subsequent degeneration (Mitchell and Lee, 2012).

Methods

Animals

All experimental procedures were reviewed and approved by the Northwestern University Institutional Animal Care and Use Committee (IACUC). Because of the reproducible and stereotyped progression of symptoms, we chose to use mSOD1 mice overexpressing SOD1(G93A), in which glycine has been substituted by alanine at residue 93. All mice had a B6SJL background (Jackson Lab, Bar Harbor, ME). The transgene copy number was compared to a housekeeping gene at Transnetyx

(Cordova, TN), and only mice with relative copy number >45 were used in this study. Control group consisted of non-transgenic littermates, with the same B6SJL background (WT). 33 animals of either sex were used in this study, and they were divided into different age groups for analysis: P30–60 (N=9 mice), P60–90 (N=12 mice), and P90–120 (N=12 mice).

In vivo preparation

Procedures were similar to those in our previous studies (Manuel and Heckman, 2011). Initially, atropine (0.2mg/kg) was administered subcutaneously to prevent salivation. Ten minutes later, anesthesia was initiated with an intraperitoneal injection of pentobarbital sodium (70 mg/kg) and maintained by intravenous infusion of supplemental doses of pentobarbital (6 mg/kg) mixed in perfusion solution containing 4% glucose, 1% $NaHCO_3$, and 14% Plasmion. The trachea was cannulated, allowing the mouse to be artificially ventilated with 100% O_2. The end-tidal PCO_2 was continuously monitored and maintained around 4% by adjusting ventilator parameters including respiratory rate around 120–150 bpm and tidal volume around 0.09–0.23 mL. The hind limb muscles were then dissected; biceps femoris was removed to expose the sciatic nerve, which was thereafter placed over a stimulating electrode. A laminectomy was performed at T13–L1 level, and L3–L4 spinal segments were exposed. To prevent the spinal cord from dehydration, a custom made bath was affixed using silicone elastomer and covered with mineral oil. To locate the motoneurons of interest, the sciatic nerve was stimulated at intensity 1.8× threshold for the apparition of an afferent volley.

Electrophysiology

Intracellular recordings of spinal motoneurons were performed by impaling them with glass micropipette electrodes filled with 3M KCl with resistance of 8–15 MΩ. Motoneurons were identified by the presence of antidromic action potential from stimulation of the sciatic nerve. Cells with unstable resting membrane potential (RMP) or with RMP more depolarized than −50mV were excluded from analysis.

PICs were recorded in discontinuous voltage clamp mode, with switching rates of 6–8 kHz. Clamp feedback gain was between 0.3 and 1.5. In addition to the feedback gain from Axoclamp amplifier, an additional low-frequency feedback loop with a gain of 11 and a cutoff of −3 dB at 0.3 kHz was used to improve voltage control in such large cells as motoneurons (Lee and Heckman, 1998). Outputs were observed at all times to assure reasonable settling of the electrode. To record PICs, a slow triangular voltage ramp (−80 to −40 mV) was applied (Lee and Heckman, 1998). Leak current was determined by fitting a regression line through the subthreshold region of the I-V function. Then, this leak was subtracted from the total function to determine the PIC amplitude (measured both on the ascending and descending part of the ramp). In addition, the voltage at which the PIC was maximal on each part of the ramp was recorded (PIC peak voltage), as well as the voltage at which the current trace deviated from the leak current (PIC onset voltage) on the ascending ramp, and joined back the leak trace on the descending ramp (PIC end voltage). Input conductance was estimated as the slope of the leak current.

To assess intrinsic properties of the motoneuron in current clamp mode, we measured the frequency-current (F-I) relationship of action potential firing. The F-I relationship was determined based on the firing produced by a triangular current injection. The interspike frequency was then plotted against the intensity of the injected current. All these measurements were carried out in the discontinuous current clamp mode of the Axoclamp 2A amplifier, with switching rates of 6–8 kHz. Mouse motoneurons possess two regimes of firing: a sub-primary range of firing, followed by a linear primary range (Manuel et al., 2009; Manuel and Heckman, 2011). The "gain" of the F-I relationship was determined by fitting a regression line over the linear primary range (separately on the ascending and descending phase of the ramp). The other parameters measured in the F-I relationship were: the current at which the first action potential (AP) fires on the ascending ramp (recruitment current). the current at which the last AP fires on the descending ramp (current at de-recruitment); the voltage threshold for spiking, which was determined as the voltage where the slope of the membrane voltage reaches 10mV/s before the first AP (Sekerli et al., 2004); the current and firing frequency at the transition between the sub-primary and primary ranges (Manuel and Heckman, 2011).

Data analysis

Recordings were acquired and analyzed using Spike2 v.7 (CED, Cambridge, UK). Data were collected and analyzed using Pandas v.1.0.0 (McKinney, 2011), SciPy Python v.1.4.1 (Virtanen et al., 2020) and DABEST v.0.3.0 (Ho et al., 2019). Figures were generated using matplotlib v.3.1.3 (Hunter, 2007) and seaborn v.0.10.0 (Waskom et al., 2020).

Statistics

All data are reported as mean ± standard deviation with their respective sample size. When comparing between WT and mSOD1 samples, we focus on estimation statistics that rely on effect sizes and confidence intervals (95%CI), rather than null hypothesis significance testing, as recommended by several scientific societies and editorial boards (Bernard, 2019; Makin and Orban de Xivry, 2019; Wasserstein et al., 2019; Michel et al., 2020). Unless otherwise specified, effect sizes are reported as difference of means and Hedges' g (Hedges, 2016), as calculated using DABEST v.0.3.0. (Ho et al., 2019). Where appropriate, data are presented as Cumming plots (Cumming, 2012) generated using DABEST. In these plots, the raw data are plotted as swarms of points. In addition, the mean ± standard deviation of each group is plotted as a notched line immediately to the right of each group. The effect size and bootstrapped 95% CIs are plotted on a separate axes beneath the raw data. Confidence intervals were bias-corrected and accelerated, and are displayed with the bootstrap distribution of the mean; resampling was performed 5000 times (Ho et al., 2019). Welch's *t*-test (Welch, 1947) results are provided for information only.

Results

Motoneurons from young adult mutant mice have overly large PICs

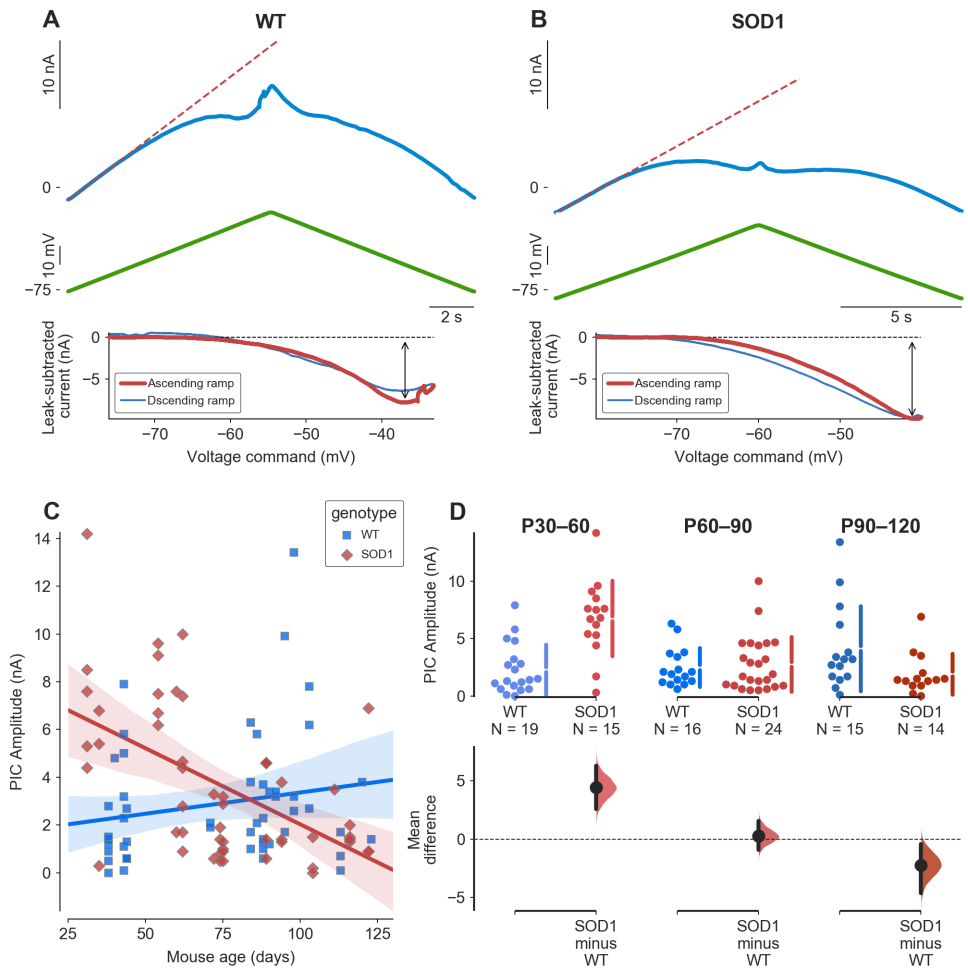

Figure 1: PIC amplitude is larger is young adult mSOD1 mice
A. Example of a PIC recording from a P43 WT mouse. Top trace: recorded current, bottom trace: voltage command. The red dashed line shows the leak current estimated by fitting a straight line around the point of zero current, and which is used to measure the input conductance of the cell. Below is a plot of the leak-subtracted current vs. the voltage command color coded for the ascending phase (thick red line) and the descending phase (thin blue line). The amplitude of the PIC is measured at the point indicated by the double arrow. Note that, in this example, a breakaway spike was filtered out. B. Example of a PIC recording from a P62 mSOD1 mouse. Same organization as in A. C. Plot of the amplitude of the PICs (in nA) vs. the age of the mouse in WT (blue square) and mSOD1 mice (red diamonds). The solid

lines correspond to the linear regression lines with 95% confidence intervals (shaded areas). Pearson correlation coefficients & 95%CI, WT: r=0.18 [−0.10–0.44] (p=0.2), mSOD1: r=−0.54 [−0.70–−0.31] (p=3.4e−5). D. Breakdown of the difference in PIC amplitude between WT and mSOD1 animals by age groups. P30–60 WT: 2.30±2.17nA, N=19 vs. mSOD1: 6.73±3.28nA, N=15; g=1.59 95%CI[0.63–2.45]; t(32)=−4.50, p=0.00016. P60–90 WT: 2.47±1.69nA, N=16 vs. mSOD1: 2.75±2.40nA, N=24; g=0.12 95%CI[−0.53–0.65]; t(38)=−0.42, p=0.67. P90–120 WT: 4.12±3.69nA, N=15 vs. mSOD1: 1.90±1.78nA, N=14; g=−0.74 95%CI[−1.26–0.01]; t(27)=2.08, p=0.05.

We set out to measure persistent inward currents (PICs) in 103 motoneurons from SOD1(G93A) mice (mSOD1), and their non-transgenic (WT) littermate, aged between 31 and 123 days old. PICs were measured in response to a slow (5 mV/s) ramp in voltage-clamp mode. The amplitude of the PIC was measured on the leak-subtracted trace at the point where the downward deflection of the trace was maximal (see Figure 1). In WT animals, the PIC amplitude remained roughly steady during the age period studied (Figure 1C). However, in mSOD1 motoneurons, PIC amplitudes decreased strikingly over time (slope=−0.45 nA/week, r=−0.54 95%CI[−0.70–−0.31], p=3.4e-5). When broken down by age groups (Figure 1D), our results shows that, in the young adult stage (P30–60), when animals are pre-symptomatic and neuromuscular-junction denervation is just starting, SOD1 mutation lead to an almost 3× increase in PIC amplitudes compared to WT motoneurons. This increase appears to be a continuation of the trend observed in neonates, where PICs were already increased ∼2-fold compared to controls (Quinlan et al., 2011). In the presymptomatic group (P60–90), however, this effect became negligible despite the fact that substantial denervation is already underway. At symptomatic stages (P90–120), the trend seen in young animals is reversed: PICs

are much smaller in mSOD1 motoneurons compared to WT motoneurons. Similar results could be observed on the PIC amplitudes measured on the descending ramp (Table 1).

In addition to its effect on PIC amplitude, SOD1 mutation also affected the voltage at which PICs are recruited. The "PIC onset voltage", measured as the voltage at the point where the leak-subtracted motoneuron I-V curve initially begins to curve downward, was hyperpolarized by 10 mV in young mSOD1 mice compared to WT controls (WT: −58.03±6.35mV, N=19 vs. mSOD1: −69.41±5.71mV, N=15; g=−1.83 95%CI[−2.64−−0.78]; $t(32)$=5.49, p=5.1e−06). The SOD1 mutation had a similarly large effect on the voltage at which the PIC reached its maximum in young animals (WT: −43.83±4.79mV, N=19 vs. SOD1: −52.32±4.20mV, N=15; g=−1.83 95%CI[−2.63−−1.04]; t(32)=5.50, p=4.8e−06). Similarly to the situation with PIC amplitude, the effect of the SOD1 mutation on its activation voltage was reduced in older animals, at both presymptomatic and symptomatic ages (Table 1).

These profound changes in PIC amplitude and activation voltage would be expected to have an impact on the firing properties of motoneurons. We therefore performed current-clamp recordings in the same motoneurons as above. We injected a triangular ramp of current to elicit the repetitive firing of the motoneuron (Figure 2A–B), and measured the voltage threshold for spiking on the first spike triggered by the ramp. In concordance with the hyperpolarization of the PICs, spiking threshold was also hyperpolarized in young animals (WT: −45.35±5.48mV,

N=19 vs. mSOD1: −54.86±5.15mV, N=14; g=−1.74 95%CI[−2.53−−0.81]; t(31)=5.10, p=1.9e−05).

Young adult motoneurons are nonetheless not hyperexcitable

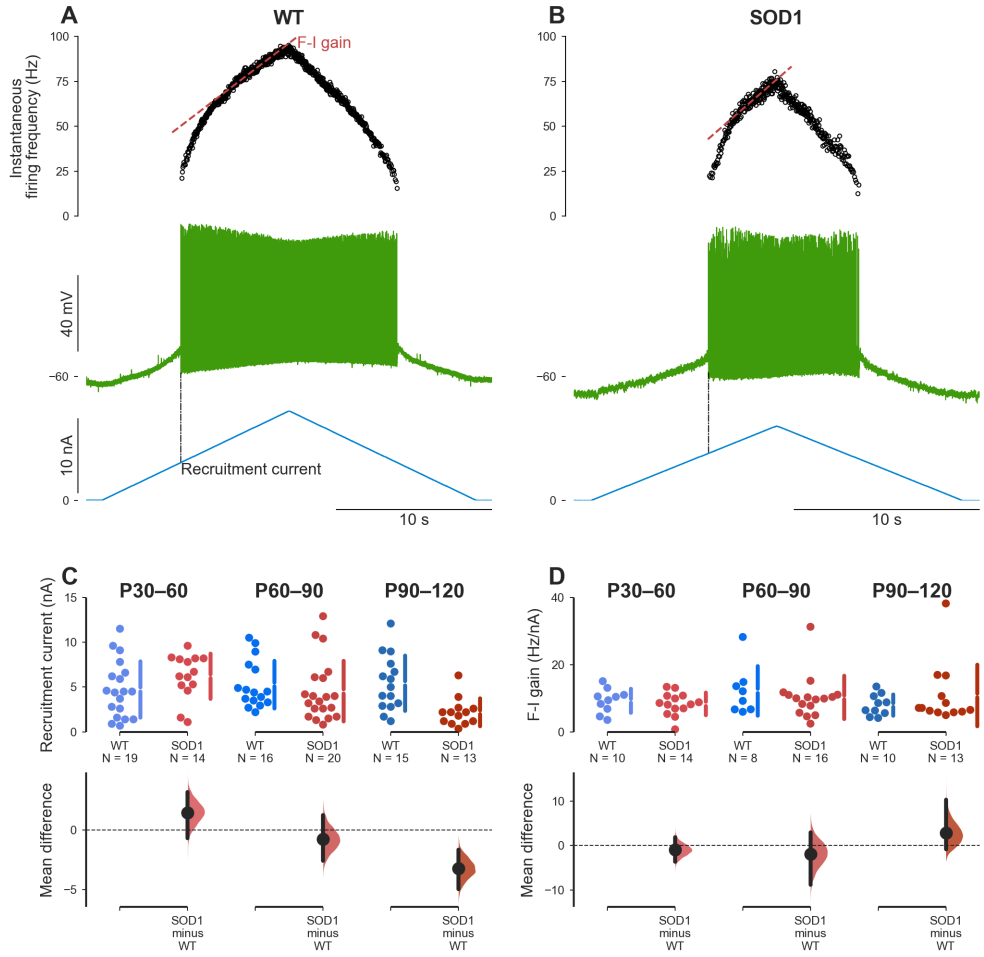

Figure 2. Mutant motoneurons are not hyperexcitable
A. Example of the response of a P101 WT mouse to a triangular ramp of current. From bottom to top, traces are: injected current, membrane potential and instantaneous firing frequency. The dash-dotted line shows the measure of the recruitment current, the current intensity at which the motoneuron starts to fire. The red dashed line shows the linear fit of the firing frequency in the primary range, used to estimate the gain of the F-I relationship. B. Example of the response of a P60 mSOD1 mouse. Same organization as in A. C. Current intensity required for eliciting

the first spike on a triangular ramp of current in WT and mSOD1 motoneurons in each of the age groups. In young adult and presymptomatic mice, mutant motoneurons require the same amount of current than WT motoneuron to fire, P30–60 WT: 4.73±3.14nA, N=19 vs. mSOD1: 6.21±2.51nA, N=14; g=0.50 95%CI[−0.24–1.24]; $t(31)$=−1.51, p=0.14. P60–90 WT: 5.28±2.64nA, N=16 vs. mSOD1: 4.53±3.38nA, N=20; g=−0.24 95%CI[−0.93–0.41]; $t(34)$=0.75, p=0.46. At the symptomatic stages (P90–120), mutant motoneurons exhibit a lower current threshold for firing (WT: 5.43±3.07nA, N=15 vs. mSOD1: 2.19±1.56nA, N=13; g=−1.26 95%CI[−1.95−−0.47]; $t(26)$=3.59, p=0.0017), compatible with the loss of the least excitable cells. D. The slope of the F-I relationship, measured over the primary range, is not affected by the mutation. P30–60 WT: 9.3±3.6Hz/nA, N=10 vs. mSOD1: 8.3±3.4Hz/nA, N=14; g=−0.28 95%CI[−1.10–0.64]; $t(22)$=0.69, p=0.5. P60–90 WT: 12.2±7.3Hz/nA, N=8 vs. mSOD1: 10.3±6.4Hz/nA, N=16; g=−0.27 95%CI[−1.22–0.54]; $t(22)$=0.62, p=0.54. P90–120 WT: 8.0±3.2Hz/nA, N=10 vs. mSOD1: 10.8±9.1Hz/nA, N=13; g=0.38 95%CI[−0.43–0.93]; $t(21)$=−1.04, p=0.31.

Despite the large alterations in PIC amplitude and activation voltage, and despite the change in the voltage threshold for spiking, the excitability of the motoneurons was remarkably unaffected by the SOD1 mutation, regardless of age. Figure 2 shows the response of WT and mSOD1 young adult motoneurons to a slow triangular ramps of current (F-I relationship). We measured the intensity of the current required to elicit the first spike on the ascending ramp ("recruitment current"). Young adult (P30–60) mutant motoneurons, whose neuromuscular junctions are just starting to be denervated, and pre-symptomatic motoneurons (P60–90), which experience substantial denervation, did not require, on average, less current to reach firing threshold than WT controls (Figure 2C). At symptomatic stages (P90–120), the SOD1 mutation does lead to a decrease in the recruitment current compared to WT animals (Figure 2C), which is probably caused by the degeneration of the high threshold motoneurons at this stage.

As shown previously (Manuel et al., 2009), most F-I curves, regardless of age and genotype, showed a distinct sub-primary range (SPR) with a steep slope followed by a linear phase called primary range (PR). We used the "gain" of the motoneuron, i.e. the slope of the F-I curve in the PR, as another measure of excitability of motoneurons. Despite the alterations in PICs in mutant motoneurons, the gain of the motoneuron F-I curves were unaffected by both age and mutation (Figure 2D).

Compensatory changes responsible to maintain excitability

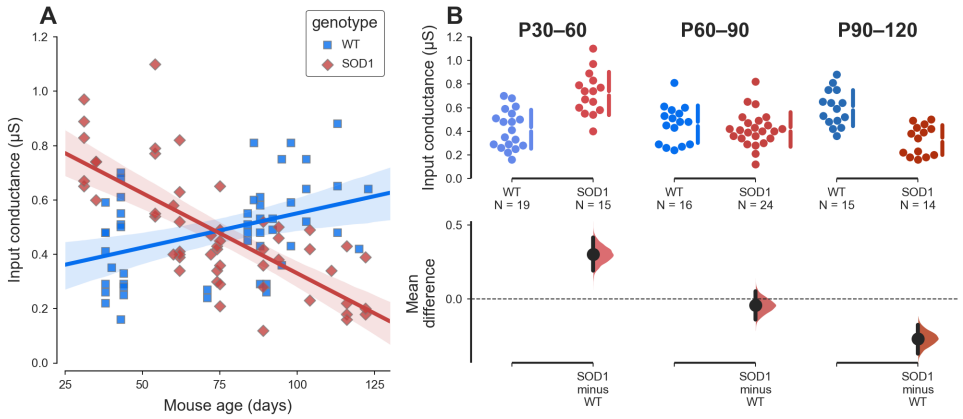

Figure 3: Young mutant motoneurons have an aberrantly large input conductance

A. Plot of the motoneuron input conductance vs. age in WT (blue squares) and mSOD1 (red diamonds) animals. The solid lines correspond to the linear regression lines with 95% confidence intervals (shaded areas). Pearson correlation coefficients & 95%CI, WT: r=0.40 95%CI[0.14–0.61], p=0.0035, mSOD1: r=−0.73 95%CI[−0.83–−0.57], p=6.1e−10. B. Breakdown of the difference in input conductance between WT and mSOD1 animals by age groups. P30–60 WT: 0.42±0.16µS, N=19 vs. mSOD1: 0.72±0.18µS, N=15; g=1.73 95%CI[0.92–2.41]; t(32)=−5.06, p=2.2e−05. P60–90 WT: 0.46±0.16µS, N=16 vs. mSOD1: 0.42±0.15µS, N=24; g=−0.28 95%CI[−0.96–0.37]; t(38)=0.88, p=0.39. P90–120 WT: 0.60±0.15µS, N=15 vs. mSOD1: 0.33±0.13µS, N=14; g=−1.85 95%CI[−2.57–−1.16]; t(27)=5.16, p=2.1e−05.

The fact that young adult motoneurons are not hyperexcitable despite substantial alteration in the PICs suggests that other compensatory mechanisms are acting to preserve the functional output of the cells. Motoneuron input conductance is an

important factor controlling neuron excitability. We estimated the input conductance of mSOD1 and WT motoneurons from the slopes of their I-V relations around the level of the resting membrane potential (see Figure 1 and Methods). Input conductances of mSOD1 and WT motoneurons were plotted against the age of the animal in Figure 3A. Consistent with the continuous increase in size of the animals over the age span studied, WT motoneurons exhibit a moderate increase in input conductance in WT motoneurons over time (slope=0.02 μS/week). On the other hand, mSOD1 motoneurons showed the opposite trend (slope=−0.04 μS/week). Young adult mutant motoneurons had an input conductance almost twice as high as WT controls at P30–P60 (Figure 3B). This increase is relatively greater (～1.7 fold) than that observed in neonatal motoneurons at P0–7 (～1.25 fold) (Quinlan et al., 2011), suggesting that the trend for increased conductance has become stronger as the animal matures into the young adult state. However, by the late pre-symptomatic stage (P60–90), the mutation had no longer any effect on input conductance. Finally, symptomatic (P90–120) mSOD1 motoneurons had a smaller input conductance than WT controls, but this difference could be due to the degeneration of the largest, high-threshold units at this stage.

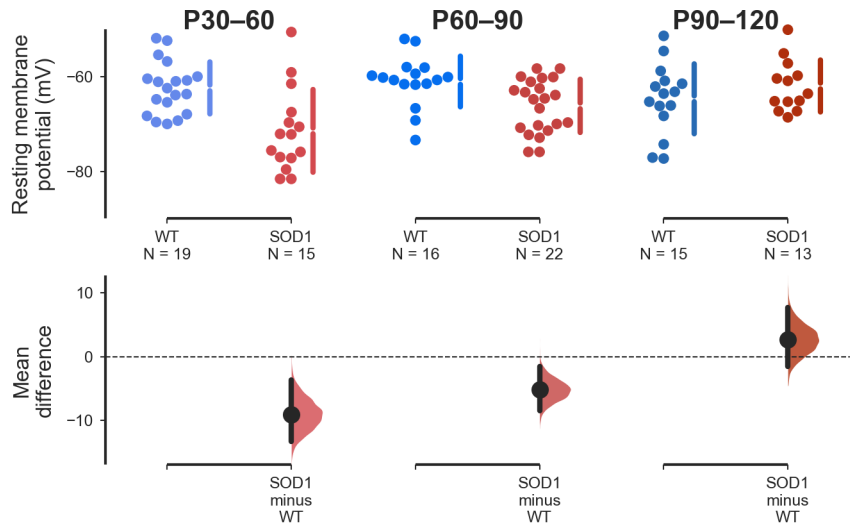

Figure 4. The resting membrane potential of young adult mutant mice is hyperpolarized

Breakdown of the difference in input conductance between WT and mSOD1 animals by age groups. P30–60 WT: −62.38±5.52mV, N=19 vs. mSOD1: −71.45±8.78mV, N=15; g=−1.24 95%CI[−2.13–−0.23]; $t(32)$=3.49, p=0.002. P60–90 WT: −60.98±5.35mV, N=16 vs. mSOD1: −66.18±5.63mV, N=22; g=−0.92 95%CI[−1.54–−0.18]; $t(36)$=2.89, p=0.0067. P90–120 WT: −64.71±7.42mV, N=15 vs. mSOD1: −61.99±5.43mV, N=13; g=0.40 95%CI[−0.35–1.10]; $t(26)$=−1.12, p=0.27.

The increase in input conductance is not the only compensatory change happening in young adult mutant motoneurons. In particular, one would have expected the leftward shift in the activation voltage of PICs seen in these motoneurons to have a profound impact on their firing behavior. This discrepancy can be explained by a parallel almost 10 mV hyperpolarization of the resting membrane potential in young adult mSOD1 motoneurons (Figure 4, P30–60). This effect is still observable at pre-symptomatic stages, but to a lesser degree (Figure 4, P60–90). At symptomatic ages, however, mutant motoneurons had similar resting membrane potentials as WT controls (Figure 4, P90–120).

When taking into account this hyperpolarization of the resting membrane potential, the relative values of the voltage threshold for spiking (ΔV_{th}, difference between the voltage threshold and the resting membrane potential), as well as the relative activation voltage of the PICs (ΔV_{PIC}) and the relative voltage at the peak of the PIC (ΔV_{peak}) were all similar between WT and mSOD1 motoneuron regardless of age (Table 1), which suggest that these are the quantities that are homeostatically regulated.

Arms race between PICs and input conductance

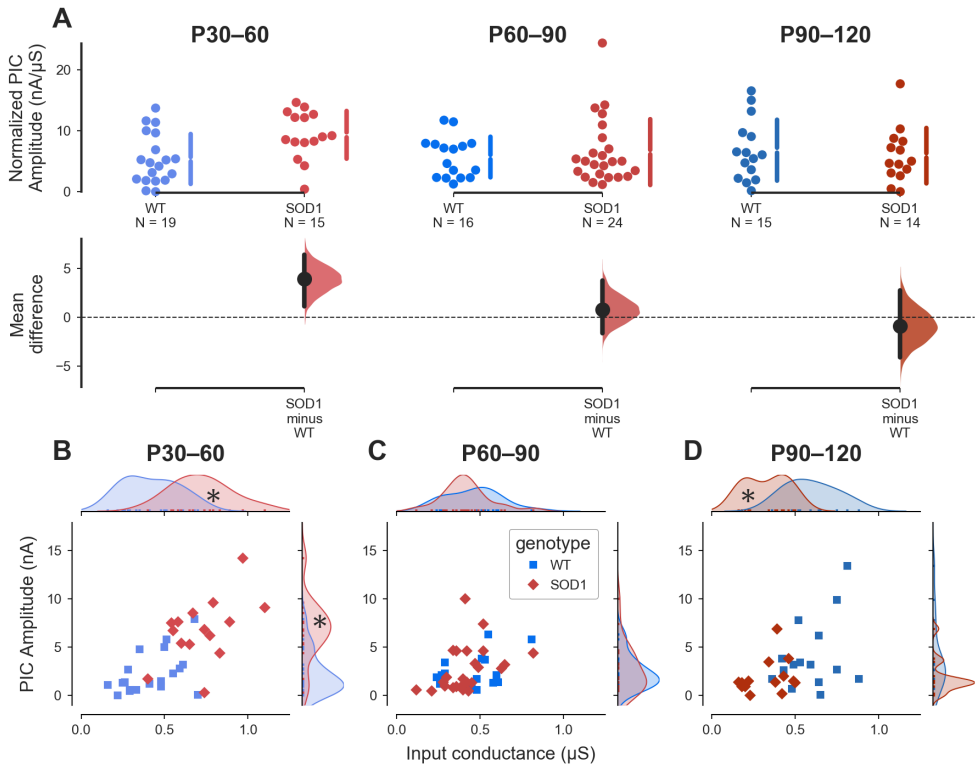

Figure 5. Some motoneurons exhibit properties outside of the normal range
A. Breakdown of the difference in normalized PIC amplitude (PIC amplitude divided by input conductance) between WT and mSOD1 animals by age groups. P30–60 WT: 5.35±4.11nA/μS, N=19 vs. mSOD1: 9.32±3.94nA/μS, N=15; g=0.96 95%CI[0.16–1.76]; $t(32)$=−2.86, p=0.0075. P60–90 WT: 5.65±3.35nA/μS, N=16 vs. mSOD1:

6.46±5.39nA/μS, N=24; g=0.17 95%CI[−0.50–0.66]; t(38)=−0.59, p=0.56. P90–120 WT: 6.80±5.01nA/μS, N=15 vs. mSOD1: 5.93±4.53nA/μS, N=14; g=−0.18 95%CI[−0.88–0.63]; t(27)=0.49, p=0.63. B. Plot of the PIC amplitude vs. the input conductance of young adult motoneurons (P30–60) in WT (blue squares) and mSOD1 (red diamonds) animals. The marginal plots indicate the kernel density estimation of the distributions of the values in the two populations. The asterisks indicate point to fraction of the mSOD1 population that is outside the range of the WT population. C. Same as A for the presymptomatic age range P60–90. D. Same as A for the symptomatic age range P90–120.

Our results show that, during the disease progression, motoneurons are actively engaged in a homeostatic process to maintain their firing output. It is plausible that this process would, by itself, cause undue stress to the cell. For example, the ratio of PIC to conductance is a major determinant of net excitability (Huh et al., 2017). If these two parameters grow in proportion, then net excitability is likely to stay about the same. We thus analyzed PIC amplitudes normalized by input conductances (Figure 5A). Although pre-symptomatic and symptomatic cells manage to maintain a normal normalized-PIC amplitudes, young adult mSOD1 motoneurons have a larger normalized PIC amplitude than their WT controls (Figure 5A). This implies that, in these animals, the cells that are abnormally large (large input conductance) also have PICs that are larger than expected for their size. It is likely that these cells are under considerable stress to respond to the high metabolic demand imposed by their large size, as well as the potential massive influx of calcium caused by their abnormally large PICs.

This effect is also visible in the plots of Figure 5B–D showing the relationship between PIC amplitude and input conductance. In the young adult animals (Figure 5B), the majority of the mutant motoneurons are clustered in the upper right hand

corner, with values of both conductances and PIC amplitudes that are outside of the range of WT controls. At the pre-symptomatic stages, the WT and mSOD1 populations roughly overlap (Figure 5C), and at the symptomatic ages, the situation is reversed, with the appearance of a cluster (N=6) of very small cells (asterisk in Figure 5D), most of which also have very small PICs. These results show that the overall initial increase in PIC and conductance amplitudes driven by the SOD1 mutation generates a sub-population of motoneurons with conductance and PIC amplitudes that are actually above those of the normal, WT range (P30–60). The steady reduction in these amplitudes is so strong that by P90–120, a sub-population develops that falls below the normal range.

Hypoexcitable cells

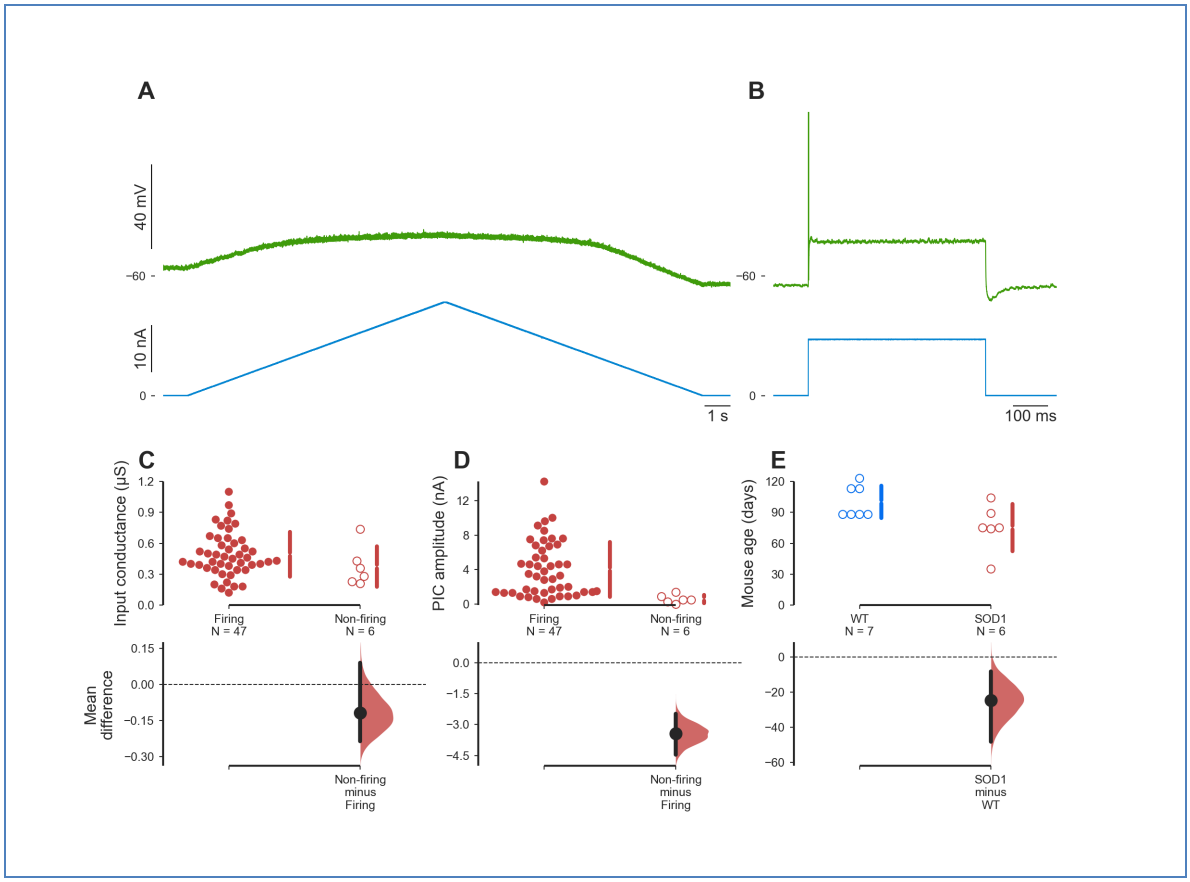

Figure 6: Some cells are hypoexcitable and cannot fire repetitively
A. Example of a mSOD1 motoneuron (from a P88 mouse) that is unable to fire repetitively in response to a triangular ramp of current. Top trace: membrane potential, bottom trace: injected current. B. This same motoneuron was able to generate a single full-height action potential in response to a square pulse of current. Same organization as in A. C. Non-firing motoneurons had a similar input conductance compared to motoneurons that were able to fire repetitively. Firing: 0.49±0.22µS, N=47 vs. non-firing: 0.38±0.20µS, N=6; g=−0.54 95%CI[−1.11–0.50]; t(51)=1.36, p=0.22 D. Non-firing motoneurons had much smaller PICs than motoneurons able to fire repetitively. Firing: Firing: 4.04±3.18nA, N=47 vs. non-firing: 0.60±0.49nA, N=6; g=−1.12 95%CI[−1.42−−0.86]; t(51)=6.81, p=1.3e−08 E. Non-firing motoneurons appear earlier in mSOD1 animals compared to WT animals. WT: 100±16 days old, N=7 vs. SOD1: 75±23 days old, N=6; g=−1.20 95%CI[−2.06–0.01]; t(11)=2.24, p=0.053

As previously shown (Delestrée et al., 2014; Martínez-Silva et al., 2018), mSOD1 motoneuron tend to lose their ability to fire repetitively as the disease progresses. In the present study, out of the 53 mutant motoneurons recorded, 6 motoneurons could not fire repetitively to current ramps despite still being able to fire a single or a few action potentials to current steps. Figure 8 shows an example of such a motoneuron. Although those cells were not, on average, larger than those that fired repetitively (Figure 6B), non-firing cells were characterized by a very PIC amplitude (Figure 6C, see also (Huh et al., 2017)). Even more striking were the difference in PIC amplitude normalized by the input conductance of the cells. Non-firing motoneurons had a much smaller normalized PIC amplitude (1.91±1.82nA/µS, N=6) compared to repetitively firing motoneurons (7.80±4.79nA/µS, N=47; g=−1.27 95%CI[−1.65−−0.80]; t(51)=5.77, p=2.6e−05). Finally, although some non-firing motoneurons could be found in WT mice, non-firing motoneurons appear on average 25 days earlier in mSOD1 mice (Figure 6D).

Table 1: summary of the properties of the motoneurons, broken down by age range

The table shows the various properties that were measured in each motoneuron. The rows are sorted in descending order of effect size at P30–60. WT and mSOD1 columns show mean values ± standard deviation, with the 95%CI around the mean below. The "Mean diff." column shows the mean difference between mSOD1 and WT population, with 95% CI below. The "Hedges' *g*" column shows a graphical representation of the effect size. ΔF: difference between the instantaneous firing frequency at de-recruitment and at recruitment. ΔI: difference between the de-recruitment and recruitment currents. ΔV_{th}: voltage threshold for spiking relative to the resting membrane potential. ΔV_{PIC}: PIC onset voltage relative to the resting membrane potential. ΔV_{peak}: voltage at the peak of the PICs relative to the resting membrane potential

Discussion

In this paper, we studied how motoneuron electrical properties evolve over the time course of ALS, focusing particularly on the persistent inward currents (PICs). We show that, in young adult mutant mice, before and up to the time where denervations are just starting, PICs are abnormally large compared to controls. This increase in PIC amplitude is accompanied by a parallel increase in motoneuron input conductance with the net effect that the excitability of the cells remains normal. Later, while the animals remain pre-symptomatic but denervation has begun, motoneuron properties return to normal levels. Finally, in symptomatic animals, mutant motoneurons tend to have smaller input conductance and smaller recruitment current.

Homeostatic regulation of motoneuron output

Although ALS is classically considered an adult-onset disease, we know from earlier studies of motoneurons in animal models of ALS that the change in motoneurons' intrinsic excitability is the first sign to be seen in the pathogenesis, long before any overt motor deficits manifest. Hyperexcitability is observed in

cultured E13 spinal motoneurons (Kuo et al., 2004), E15 cortical motoneurons (Pieri et al., 2009), E17.5 spinal motoneurons (Martin et al., 2013 p.20), as well as early postnatal hypoglossal motoneurons (van Zundert et al., 2008). Consequently, the motor system in general, and motoneurons in particular, must exhibit remarkable capability for homeostatic regulation to maintain a quasi-normal motor output until overt symptoms appear, but there are many combinations of intrinsic properties that can produce the same firing pattern (Marder and Goaillard, 2006). In neonatal mSOD1 mice, the majority of motoneurons exhibited normal excitability (based on recruitment current and F-I gain), although the most resistant population of motoneuron seem to retain some hyperexcitability (Quinlan et al., 2011; Leroy et al., 2014). Yet, PICs were almost twice as large in mutant compared to WT neonatal motoneurons. This increased PIC amplitude was seemingly compensated by a parallel increase in input conductance (Quinlan et al., 2011). In young adult animals, this trend seems to continue, as the present study demonstrated an almost 3× increase in PIC amplitude, accompanied by an almost 2× increase in input conductance. Similarly, we observed large changes in PIC onset and peak voltages, compensated by a commensurate hyperpolarization of the resting membrane potential. These trends with disease progression from the neonatal state through development of severe symptoms are summarized in Figure 7. An overall pattern of oscillations is evident, with the PIC oscillations tending to increase excitability but the conductance and rest potential oscillations tending to reduce it.

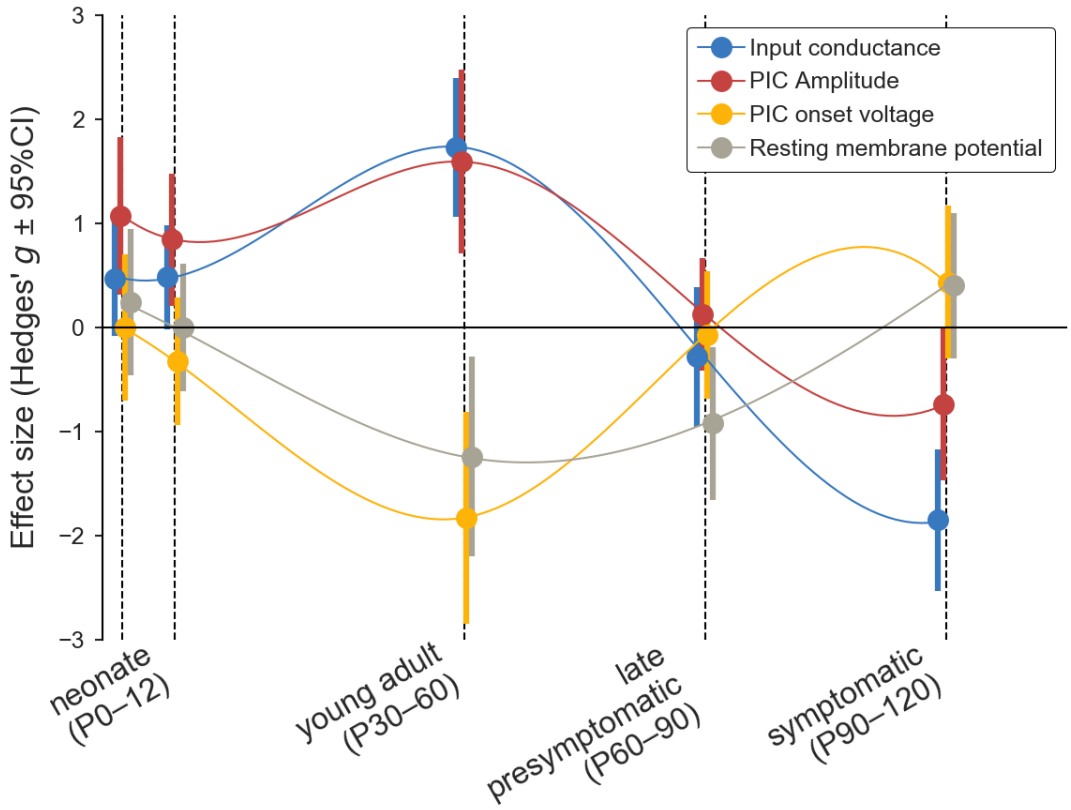

Figure 7: summary of the changes in motoneuron properties over time
Schematic representation of the changes in four key electrophysiological properties over time. The dots represent the effect size (Hedges' g) and the vertical bars show the 95%CI around g. The thin lines are cubic splines interpolation of the data over time. The points have been slightly staggered so that the vertical bars do not occlude each other. Data from neonates (P0–5 and P6–12) are from Quinlan et al. (2011).

The properties of the motoneurons seem to normalize at the late pre-symptomatic stage (P60–90), but it is unclear whether this is due to changes in the homeostatic pathways involved, or whether it is caused by the start of the degeneration process in the most vulnerable motoneurons. At symptomatic stages, motoneurons appear to be hypoexcitable. They have a smaller input conductance (Figure 3), and smaller recruitment current (Figure 2), but that most likely reflect the fact that the largest cells have degenerated by this age, and that the remaining cells may have shrunk (see below, and Dukkipati et al., 2018).

The hidden cost of homeostatic regulation

Although the degeneration of motoneurons in ALS constitutes a failure in cell homeostasis, our results show that, throughout the "silent", presymptomatic phase of ALS, motoneurons are actively engaged in a highly successful homeostatic process to maintain their firing output. However, this process is not perfect, and, by itself, could be a major source of stress for the cells. We do not know whether the cells increase their conductance to compensate for the fast increase in PICs or *vice versa*, but the end result is the appearance of cells with both input conductance and PIC amplitudes outside of the normal range (Figure 5B). The increase in input conductance could be due to the insertion of more channels in the membrane. However, direct measurements of soma sizes have revealed that pre-symptomatic mutant cells are physically larger than controls (Shoenfeld et al., 2014; Dukkipati et al., 2018). This increase in size, coupled with the larger calcium entry in the cells due to the larger PICs (which are in part calcium-medicated (Li and Bennett, 2003)), is bound to cause undue metabolic stress on those cells that are outside of the normal range, despite the fact that cells manage to maintain a normal output. These cells are likely to be Fast Fatigable (FF) motoneurons, as they are the cells with the largest input conductance, and the largest PICs (Lee and Heckman, 1998; Huh et al., 2017) in normal conditions, and they are the cells that are the most vulnerable to ALS (Pun et al., 2006; Hegedus et al., 2007, 2008).

As the disease progresses, those large, vulnerable cells become the first motoneurons that will embark on a degeneration pathway (Saxena et al., 2009, 2013; Martínez-Silva et al., 2018), and will lose their ability to fire repetitively

(Martínez-Silva et al., 2018). This early loss of the large cells is consistent with stress induced by aberrantly large conductances and PICs. This loss is also likely the primary reason why motoneurons appear to recover normal properties at late pre-symptomatic stages. Nevertheless, it is probable that all motoneurons, regardless of type, experience this form of stress. Interestingly, we observed that some of the smallest motoneurons, which are the most resistant to the disease, appear to shrink in the oldest animals (Figure 5D), consistent with anatomical observations (Kiernan and Hudson, 1991; Dukkipati et al., 2018). At this point, it is unclear whether this shrinkage is a pathological feature or a strong homeostatic effort by the surviving motoneurons to counteract the stress generated by their initial hypertrophy.

Hyper-vigilant homeostasis

Mitchell and colleagues have recently proposed that cellular homeostasis is in ALS motoneurons is in fact too strong (Mitchell and Lee, 2012; Irvin et al., 2015). Several aspects of our results are consistent with this hyper-vigilant homeostasis hypothesis. A major impetus for this hypothesis was that meta-analyses of data obtained from many studies on multiple cellular properties revealed patterns of oscillations as the disease progressed, suggesting the existence of high feedback gains for homeostatic processes. Similar oscillations are clearly present in our results, as illustrated in Figure 7. The highly successful homeostasis for net excitability, achieved at the cost of excessively high amplitudes for conductances and PICs, clearly shows homeostasis is strong. The development of subpopulations that are initially well above and then well below the normal range supports the possibility that this strong homeostasis is excessive. Direct tests of the hyper-

vigilant homeostasis hypothesis will require quantitative comparisons of the responses of ALS and WT motoneurons to controlled homeostatic challenges.

Comparison with previous studies

The present study displays some differences with other studies, including by our own group (Delestrée et al., 2014; Martínez-Silva et al., 2018). We have previously studied the properties of motoneurons in the same SOD1(G93A) mouse model of ALS but have mainly focused on a short period of time just at the onset of denervations (P45–55). Although that time point partly overlaps with the present young adult stage, we had not detected differences in input conductances (Martínez-Silva et al., 2018). This might be due to the fact that the difference in input conductance is largest at earlier time points (Figure 3A). Indeed, the difference is gone at P60–90, and we did report an increase in input conductance in an earlier series of experiments, which was more pronounced at younger time points (Delestrée et al., 2014). Similarly, we did not detect a difference in resting membrane potential in the Martínez-Silva et al. (2018) study. Again, the discrepancy could be due to the difference in the distributions of the ages of the animals studied. It is also possible that, despite our best efforts, the disease is not following the exact same time course in the two colonies used (the present paper is based on animals bred at Northwestern University in Chicago, while our previous studies were conducted on animals bred in Paris). It is therefore conceivable that even though the ages overlap, those ages correspond to slightly different stages of the disease.

In the present study, we recorded only 13 motoneurons out of 103 (7/50 WT and 6/53 mSOD1) that were unable to fire repetitively, contrary to our previous study

where we showed that a large proportion of vulnerable motoneurons became hypoexcitable before the onset of denervation (P45–55, Martínez-Silva et al., 2018). This discrepancy could be explained by the experimental constraints of the present study. Indeed, obtaining stable voltage clamp recordings in vivo in mice is quite a challenge, requiring electrodes able to pass very large amounts of current and motoneuron able to withstand the protocol. Since we have only included for analysis cells in which the voltage clamp protocol was completed successfully, we hypothesize that we may have biased our sample towards the healthiest cells that have yet to take the path of degeneration.

Limitations

The results presented here have been collected on the SOD1(G93A) mouse model of ALS, a model that has attracted criticisms due to it being an overexpression model, and its failure to bring seemingly promising therapies to the clinic (Philips and Rothstein, 2015). Nevertheless, some parallel with other studies suggest that our results could be extended to other models. First, Meehan et al. (2010) have studied an unrelated mSOD1(G127X) model and have shown that although the net excitability of the motoneurons was not affected by the mutation, there were nonetheless signs of increased PICs in these motoneurons. Second, we observed that, in late symptomatic animals, some cells exhibited a very small input conductance, well below the normal range at this age, suggesting that these cells actually shrank. This observation matches morphological measurements in mSOD1 mice (Dukkipati et al., 2018), but also observations from sporadic human patients (Kiernan and Hudson, 1991).

We demonstrated a remarkably successful homeostatic control of motoneuron firing, that we can attribute to commensurate changes in PICs and input conductance. However, it is likely that other currents are also implicated in this process (Marder and Goaillard, 2006). Limitations inherent to in vivo electrophysiology prevent us from isolating many different currents and further in vitro investigations in adults (Jiang and Heckman, 2006; Mitra and Brownstone, 2011; Jiang et al., 2017; Bhumbra and Beato, 2018) are warranted to shed more light on the panoply of channels involved in this process.

Conclusion

Overall, our results show homeostasis for net excitability in mutant SOD1 motoneurons is remarkably strong in the presymptomatic state. This success however comes at a cost of large compensatory changes in basic electrical properties. These results support the hypothesis that ALS is not due to a single specific root cause but instead caused by an inherent instability at the system-level (Mitchell and Lee, 2012), possibly caused by an "hyper-vigilant" homeostatic system in motoneurons. Initial perturbations in the electrical properties of motoneurons would be overcompensated for, leading to new sources of stress, which, in turn, would be overcorrected, and so on and so forth until the metabolic burden becomes too high to sustain for the motoneuron. FF motoneurons have higher metabolic needs (Le Masson et al., 2014) and lower calcium-buffering capabilities (Grosskreutz et al., 2010) in the first place, which make them particularly vulnerable to this vicious cycle.

Data availability

Data files and a computational notebook allowing reproducing the analysis and figures of this article are provided at the URL:

http://doi.org/10.5281/zenodo.3831947

References

Bernard C (2019) Changing the Way We Report, Interpret, and Discuss Our Results to Rebuild Trust in Our Research. eNeuro 6 Available at: https://www.eneuro.org/content/6/4/ENEURO.0259-19.2019 [Accessed April 13, 2020].

Bhumbra GS, Beato M (2018) Recurrent excitation between motoneurones propagates across segments and is purely glutamatergic. PLOS Biol 16:e2003586 Available at: https://journals.plos.org/plosbiology/article?id=10.1371/journal.pbio.2003586 [Accessed May 7, 2020].

Brownstone RM, Lancelin C (2018) Escape from homeostasis: spinal microcircuits and progression of amyotrophic lateral sclerosis. J Neurophysiol 119:1782–1794 Available at: https://www.physiology.org/doi/full/10.1152/jn.00331.2017 [Accessed October 25, 2018].

Cumming G (2012) Understanding the new statistics: effect sizes, confidence intervals, and meta-analysis. New York: Routledge, Taylor & Francis Group.

Delestrée N, Manuel M, Iglesias C, Elbasiouny SM, Heckman CJ, Zytnicki D (2014) Adult spinal motoneurones are not hyperexcitable in a mouse model of inherited amyotrophic lateral sclerosis. J Physiol 592:1687–703 Available at: http://www.ncbi.nlm.nih.gov/pubmed/24445319.

Dukkipati SS, Garrett TL, Elbasiouny SM (2018) The vulnerability of spinal motoneurons and soma size plasticity in a mouse model of amyotrophic lateral sclerosis. J Physiol 596:1723–1745.

Grosskreutz J, van den Bosch L, Keller BU (2010) Calcium dysregulation in amyotrophic lateral sclerosis. Cell Calcium 47:165–174 Available at: https://doi.org/10.1016/j.ceca.2009.12.002.

Hedges LV (2016) Distribution Theory for Glass's Estimator of Effect size and Related Estimators: J Educ Stat Available at: https://journals.sagepub.com/doi/10.3102/10769986006002107 [Accessed May 7, 2020].

Hegedus J, Putman CT, Gordon T (2007) Time course of preferential motor unit loss in the SOD1 G93A mouse model of amyotrophic lateral sclerosis. Neurobiol Dis 28:154–164 Available at: https://doi.org/10.1016/j.nbd.2007.07.003.

Hegedus J, Putman CT, Tyreman N, Gordon T (2008) Preferential motor unit loss in the SOD1 G93A transgenic mouse model of amyotrophic lateral sclerosis. J

Physiol 586:3337–3351 Available at: https://doi.org/10.1113/jphysiol.2007.149286.
Ho J, Tumkaya T, Aryal S, Choi H, Claridge-Chang A (2019) Moving beyond P values: data analysis with estimation graphics. Nat Methods 16:565–566 Available at: https://www-nature-com.insb.bib.cnrs.fr/articles/s41592-019-0470-3 [Accessed December 30, 2019].
Huh S, Siripuram R, Lee RH, Turkin VV, O'Neill D, Hamm TM, Heckman CJ, Manuel M (2017) PICs in motoneurons do not scale with the size of the animal: a possible mechanism for faster speed of muscle contraction in smaller species. J Neurophysiol 118:93–102.
Hunter JD (2007) Matplotlib: A 2D Graphics Environment. Comput Sci Eng 9:90–95.
Ilieva H, Polymenidou M, Cleveland DW (2009) Non-cell autonomous toxicity in neurodegenerative disorders: ALS and beyond. J Cell Biol 187:761–772 Available at: https://doi.org/10.1083/jcb.200908164.
Irvin CW, Kim RB, Mitchell CS (2015) Seeking homeostasis: temporal trends in respiration, oxidation, and calcium in SOD1 G93A Amyotrophic Lateral Sclerosis mice. Front Cell Neurosci 9:248.
Jiang MC, Adimula A, Birch D, Heckman CJ (2017) Hyperexcitability in synaptic and firing activities of spinal motoneurons in an adult mouse model of amyotrophic lateral sclerosis. Neuroscience 362:33–46.
Jiang MC, Heckman CJ (2006) In vitro sacral cord preparation and motoneuron recording from adult mice. J Neurosci Off J Soc Neurosci 156:31–36 Available at: https://doi.org/10.1016/j.jneumeth.2006.02.002.
Johnson MD, Heckman CJ (2010) Interactions between focused synaptic inputs and diffuse neuromodulation in the spinal cord. Ann N Y Acad Sci 1198:35–41 Available at: https://doi.org/10.1111/j.1749-6632.2010.05430.x.
Kanning KC, Kaplan A, Henderson CE (2009) Motor neuron diversity in development and disease. Annu Rev Neurosci 33:409–440 Available at: https://doi.org/10.1146/annurev.neuro.051508.135722.
Kiernan JA, Hudson AJ (1991) Changes in Sizes of Cortical and Lower Motor Neurons in Amyotrophic Lateral Sclerosis. Brain 114:843–853 Available at: https://academic-oup-com.insb.bib.cnrs.fr/brain/article/114/2/843/263744 [Accessed April 13, 2020].
Kuo JJ, Schonewille M, Siddique T, Schults ANA, Fu R, Bär PR, Anelli R, Heckman CJ, Kroese ABA (2004) Hyperexcitability of cultured spinal motoneurons from presymptomatic ALS mice. J Neurophysiol 91:571–575 Available at: https://doi.org/10.1152/jn.00665.2003.
Le Masson G, Przedborski S, Abbott LF (2014) A Computational Model of Motor Neuron Degeneration. Neuron 83:758–760 Available at: http://www.ncbi.nlm.nih.gov/pubmed/25088365.
Lee RH, Heckman CJ (1998) Bistability in spinal motoneurons in vivo: systematic variations in persistent inward currents. J Neurophysiol 80:583–593.
Leroy F, Lamotte d'Incamps B, Imhoff-Manuel RD, Zytnicki D (2014) Early intrinsic hyperexcitability does not contribute to motoneuron degeneration in

amyotrophic lateral sclerosis. eLife 3 Available at: http://www.ncbi.nlm.nih.gov/pubmed/25313866.
Li Y, Bennett DJ (2003) Persistent sodium and calcium currents cause plateau potentials in motoneurons of chronic spinal rats. J Neurophysiol 90:857–869 Available at: https://doi.org/10.1152/jn.00236.2003.
Makin TR, Orban de Xivry J-J (2019) Ten common statistical mistakes to watch out for when writing or reviewing a manuscript Rodgers P, Parsons N, Holmes N, eds. eLife 8:e48175 Available at: https://doi.org/10.7554/eLife.48175 [Accessed October 28, 2019].
Manuel M, Heckman CJ (2011) Adult mouse motor units develop almost all of their force in the subprimary range: a new all-or-none strategy for force recruitment? J Neurosci 31:15188–15194 Available at: http://www.ncbi.nlm.nih.gov/pubmed/22016552.
Manuel M, Iglesias C, Donnet M, Leroy F, Heckman CJ, Zytnicki D (2009) Fast kinetics, high-frequency oscillations, and subprimary firing range in adult mouse spinal motoneurons. J Neurosci 29:11246–11256 Available at: http://www.ncbi.nlm.nih.gov/pubmed/19741131.
Marder E, Goaillard J-M (2006) Variability, compensation and homeostasis in neuron and network function. Nat Rev Neurosci 7:563–574.
Martin E, Cazenave W, Cattaert D, Branchereau P (2013) Embryonic alteration of motoneuronal morphology induces hyperexcitability in the mouse model of amyotrophic lateral sclerosis. Neurobiol Dis 54:116–26.
Martínez-Silva M de L, Imhoff-Manuel RD, Sharma A, Heckman C, Shneider NA, Roselli F, Zytnicki D, Manuel M (2018) Hypoexcitability precedes denervation in the large fast-contracting motor units in two unrelated mouse models of ALS Rubin LL, ed. eLife 7:e30955 Available at: https://doi.org/10.7554/eLife.30955 [Accessed February 7, 2019].
McKinney W (2011) pandas: a foundational Python library for data analysis and statistics. Python High Perform Sci Comput 14.
Meehan CF, Moldovan M, Marklund SL, Graffmo KS, Nielsen JB, Hultborn H (2010) Intrinsic properties of lumbar motor neurones in the adult G127insTGGG superoxide dismutase-1 mutant mouse in vivo: evidence for increased persistent inward currents. Acta Physiol Oxf Engl 200:361–76.
Michel MC, Murphy TJ, Motulsky HJ (2020) New Author Guidelines for Displaying Data and Reporting Data Analysis and Statistical Methods in Experimental Biology. Mol Pharmacol 97:49–60 Available at: http://molpharm.aspetjournals.org/lookup/doi/10.1124/mol.119.118927 [Accessed January 13, 2020].
Mitchell CS, Lee RH (2012) Dynamic Meta-Analysis as a Therapeutic Prediction Tool for Amyotrophic Lateral Sclerosis. In: Amyotrophic Lateral Sclerosis (Maurer M, ed). InTech. Available at: http://www.intechopen.com/books/amyotrophic-lateral-sclerosis/dynamic-meta-analysis-as-a-therapeutic-prediction-tool-for-amyotrophic-lateral-sclerosis [Accessed January 5, 2020].
Mitra P, Brownstone RM (2011) An in vitro spinal cord slice preparation for recording from lumbar motoneurons of the adult mouse. J Neurophysiol

107:728–741 Available at: https://www.physiology.org/doi/full/10.1152/jn.00558.2011 [Accessed December 6, 2018].
Philips T, Rothstein JD (2015) Rodent Models of Amyotrophic Lateral Sclerosis. Curr Protoc Pharmacol Editor Board SJ Enna Ed--Chief Al 69:5.67.1-5.67.21 Available at: https://www.ncbi.nlm.nih.gov/pmc/articles/PMC4562058/ [Accessed April 13, 2020].
Pieri M, Carunchio I, Curcio L, Mercuri NB, Zona C (2009) Increased persistent sodium current determines cortical hyperexcitability in a genetic model of amyotrophic lateral sclerosis. Exp Neurol 215:368–379 Available at: https://doi.org/10.1016/j.expneurol.2008.11.002.
Pun S, Santos AF, Saxena S, Xu L, Caroni P (2006) Selective vulnerability and pruning of phasic motoneuron axons in motoneuron disease alleviated by CNTF. Nat Neurosci 9:408–19 Available at: http://www.ncbi.nlm.nih.gov/pubmed/16474388.
Quinlan KA, Schuster JE, Fu R, Siddique T, Heckman CJ (2011) Altered postnatal maturation of electrical properties in spinal motoneurons in a mouse model of amyotrophic lateral sclerosis. J Physiol 589:2245–2260 Available at: http://eutils.ncbi.nlm.nih.gov/entrez/eutils/elink.fcgi?dbfrom=pubmed&id=21486770&retmode=ref&cmd=prlinks.
Rosen DR, Siddique T, Patterson D, Figlewicz DA, Sapp P, Hentati A, Donaldson D, Goto J, O'Regan JP, Deng H-X (1993) Mutations in Cu/Zn superoxide dismutase gene are associated with familial amyotrophic lateral sclerosis. Nature 362:59–62 Available at: https://doi.org/10.1038/362059a0.
Saxena S, Cabuy E, Caroni P (2009) A role for motoneuron subtype-selective ER stress in disease manifestations of FALS mice. Nat Neurosci 12:627–636 Available at: https://doi.org/10.1038/nn.2297.
Saxena S, Roselli F, Singh K, Leptien K, Julien J, Gros-louis F, Caroni P (2013) Neuroprotection through Excitability and mTOR Required in ALS Motoneurons to Delay Disease and Extend Survival. Neuron 80:80–96.
Sekerli M, Del Negro CA, Lee RH, Butera RJ (2004) Estimating action potential thresholds from neuronal time-series: new metrics and evaluation of methodologies. IEEE Trans Biomed Eng 51:1665–1672.
Shoenfeld L, Westenbroek RE, Fisher E, Quinlan K a, Tysseling VM, Powers RK, Heckman CJ, Binder MD (2014) Soma size and Cav1.3 channel expression in vulnerable and resistant motoneuron populations of the SOD1G93A mouse model of ALS. Physiol Rep 2:e12113 Available at: http://physreports.physiology.org/content/2/8/e12113.abstract.
van Zundert B, Peuscher MH, Hynynen M, Chen A, Neve RL, Brown RH, Constantine-Paton M, Bellingham MC (2008) Neonatal neuronal circuitry shows hyperexcitable disturbance in a mouse model of the adult-onset neurodegenerative disease amyotrophic lateral sclerosis. J Neurosci Off J Soc Neurosci 28:10864–10874 Available at: https://doi.org/10.1523/JNEUROSCI.1340-08.2008.

Virtanen P et al. (2020) SciPy 1.0: fundamental algorithms for scientific computing in Python. Nat Methods:1–12 Available at: https://www.nature.com/articles/s41592-019-0686-2 [Accessed March 1, 2020].
Waskom M et al. (2020) mwaskom/seaborn: v0.10.0 (January 2020). Zenodo. Available at: https://doi.org/10.5281/zenodo.3629446.
Wasserstein RL, Schirm AL, Lazar NA (2019) Moving to a World Beyond "p < 0.05." Am Stat 73:1–19 Available at: https://amstat.tandfonline.com/doi/full/10.1080/00031305.2019.1583913 [Accessed April 13, 2020].
Welch BL (1947) The generalisation of student's problems when several different population variances are involved. Biometrika 34:28–35.

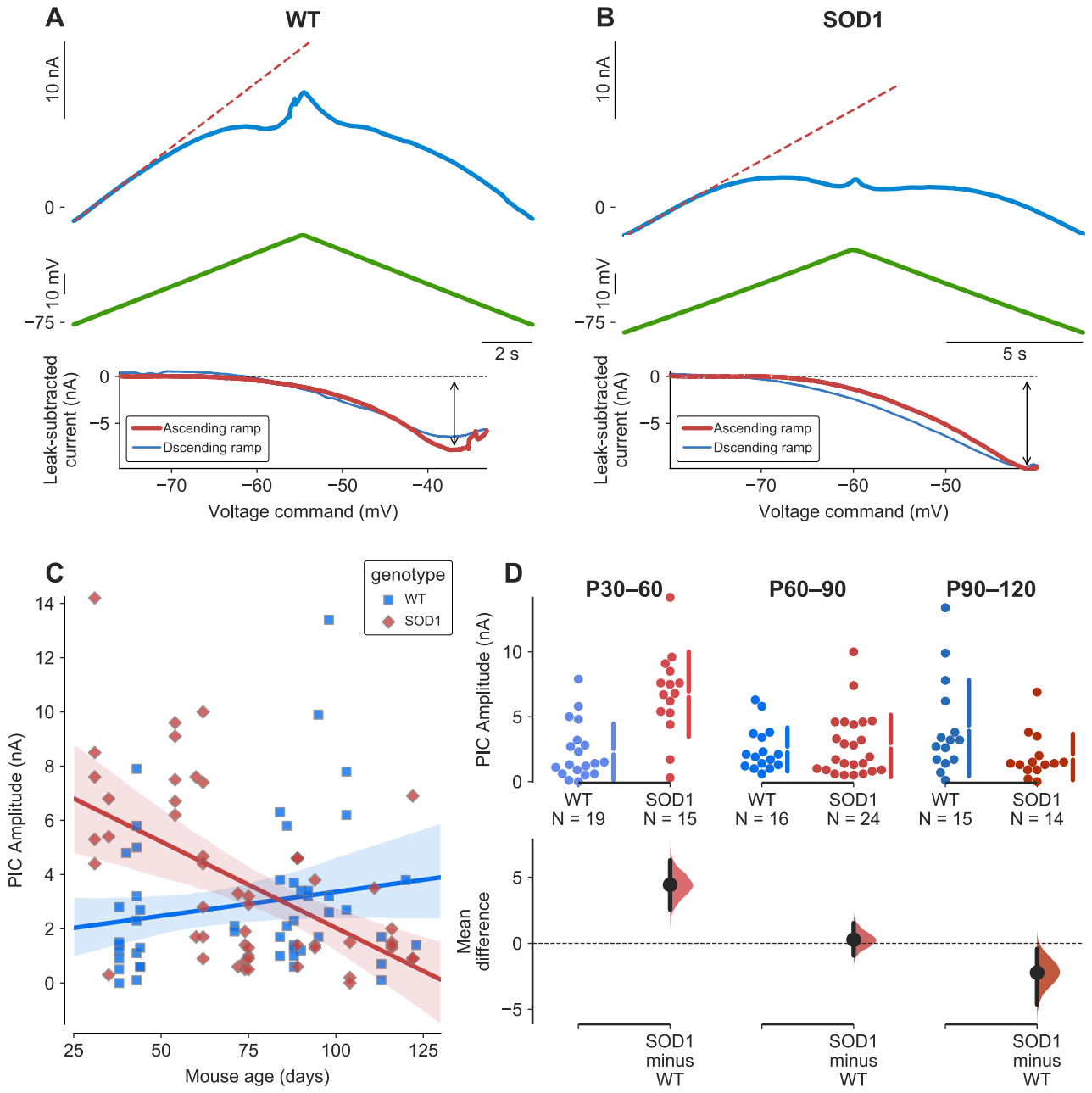
A
WT
10 nA
0
10 mV
−75
2 s
Leak-subtracted current (nA)
0
−5
Ascending ramp
Dscending ramp
−70
−60
−50
−40
Voltage command (mV)
B
SOD1
10 nA
0
10 mV
−75
5 s
Leak-subtracted current (nA)
0
−5
Ascending ramp
Dscending ramp
−70
−60
−50
Voltage command (mV)
C
genotype
WT
SOD1
PIC Amplitude (nA)
14
12
10
8
6
4
2
0
25
50
75
100
125
Mouse age (days)
D
P30–60
P60–90
P90–120
PIC Amplitude (nA)
10
5
0
WT
N = 19
SOD1
N = 15
WT
N = 16
SOD1
N = 24
WT
N = 15
SOD1
N = 14
Mean difference
5
0
−5
SOD1 minus WT
SOD1 minus WT
SOD1 minus WT

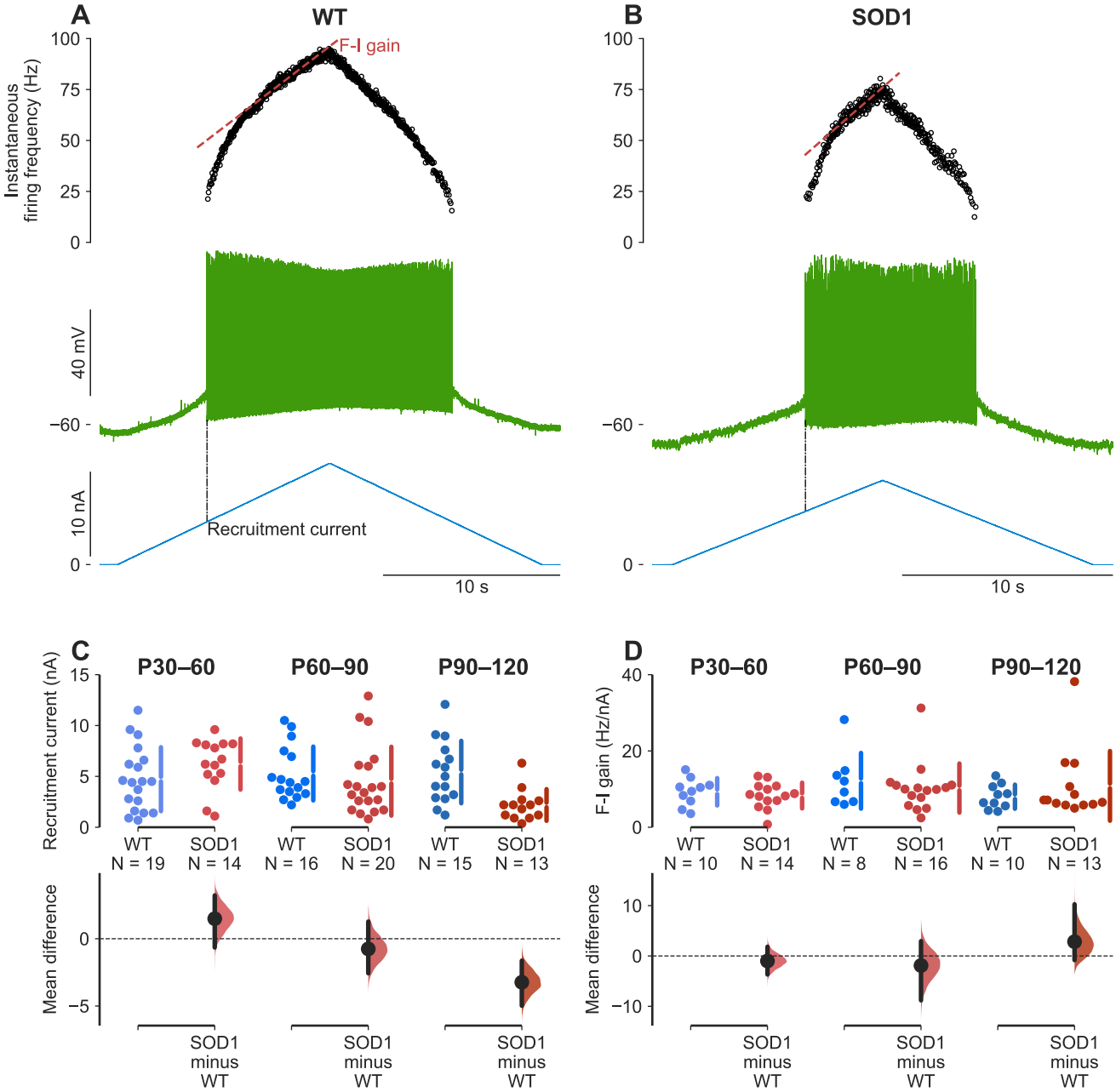
A
WT
F-I gain
Instantaneous firing frequency (Hz)
100
75
50
25
0
40 mV
−60
10 nA
0
Recruitment current
10 s
B
SOD1
100
75
50
25
0
−60
0
10 s
C
P30–60
P60–90
P90–120
Recruitment current (nA)
15
10
5
0
WT N = 19
SOD1 N = 14
WT N = 16
SOD1 N = 20
WT N = 15
SOD1 N = 13
Mean difference
0
−5
SOD1 minus WT
SOD1 minus WT
SOD1 minus WT
D
P30–60
P60–90
P90–120
F-I gain (Hz/nA)
40
20
0
WT N = 10
SOD1 N = 14
WT N = 8
SOD1 N = 16
WT N = 10
SOD1 N = 13
Mean difference
10
0
−10
SOD1 minus WT
SOD1 minus WT
SOD1 minus WT

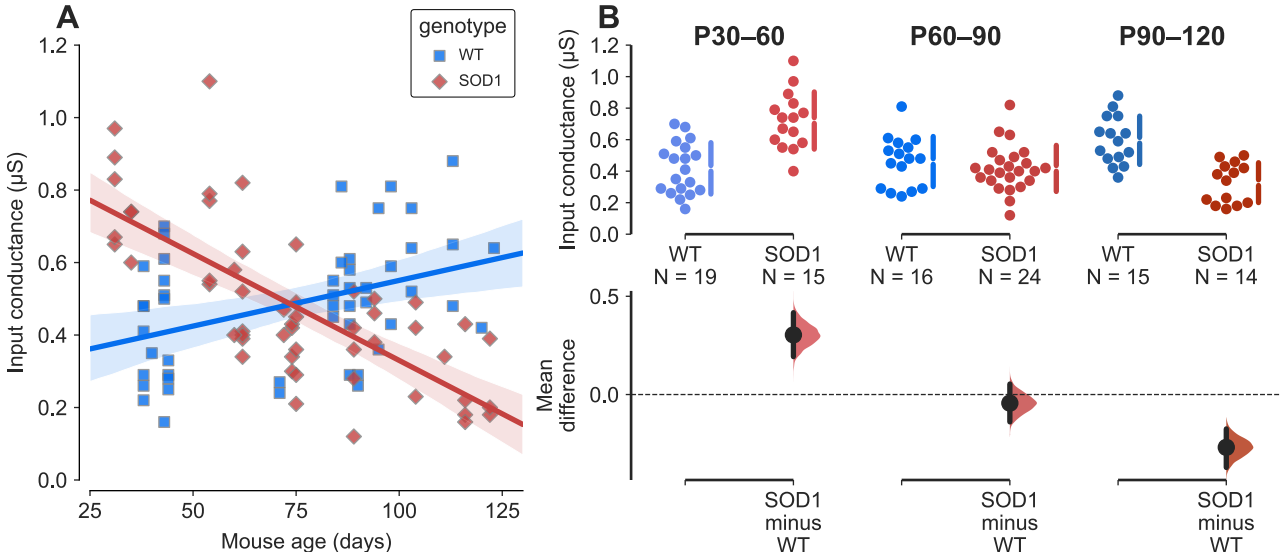
A
genotype
WT
SOD1
Input conductance (µS)
1.2
1.0
0.8
0.6
0.4
0.2
0.0
25
50
75
100
125
Mouse age (days)
B
P30–60
P60–90
P90–120
Input conductance (µS)
WT
N = 19
SOD1
N = 15
WT
N = 16
SOD1
N = 24
WT
N = 15
SOD1
N = 14
Mean difference
0.5
0.0
SOD1 minus WT
SOD1 minus WT
SOD1 minus WT

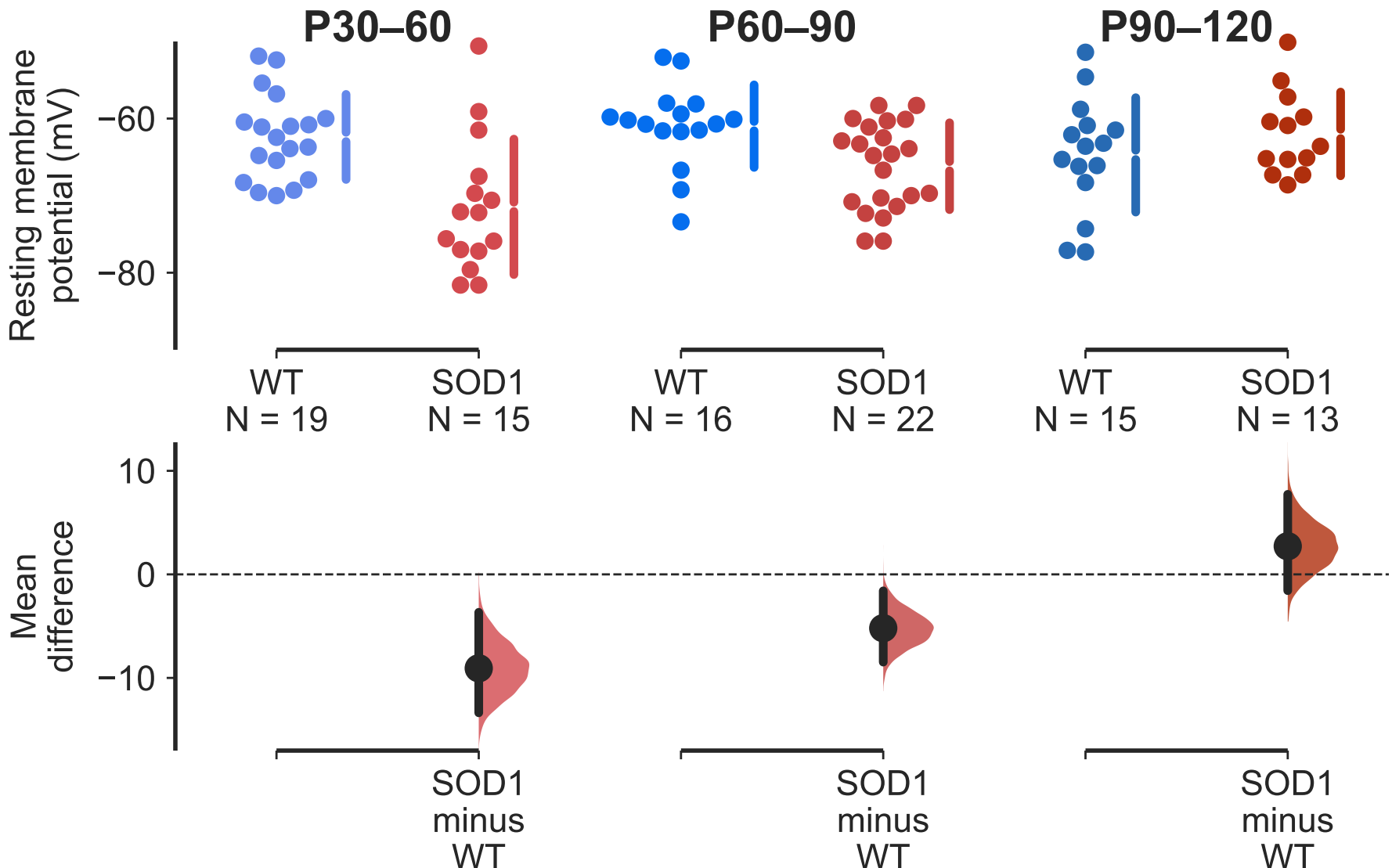
P30–60
P60–90
P90–120
Resting membrane potential (mV)
−60
−80
WT
N = 19
SOD1
N = 15
WT
N = 16
SOD1
N = 22
WT
N = 15
SOD1
N = 13
Mean difference
10
0
−10
SOD1 minus WT
SOD1 minus WT
SOD1 minus WT

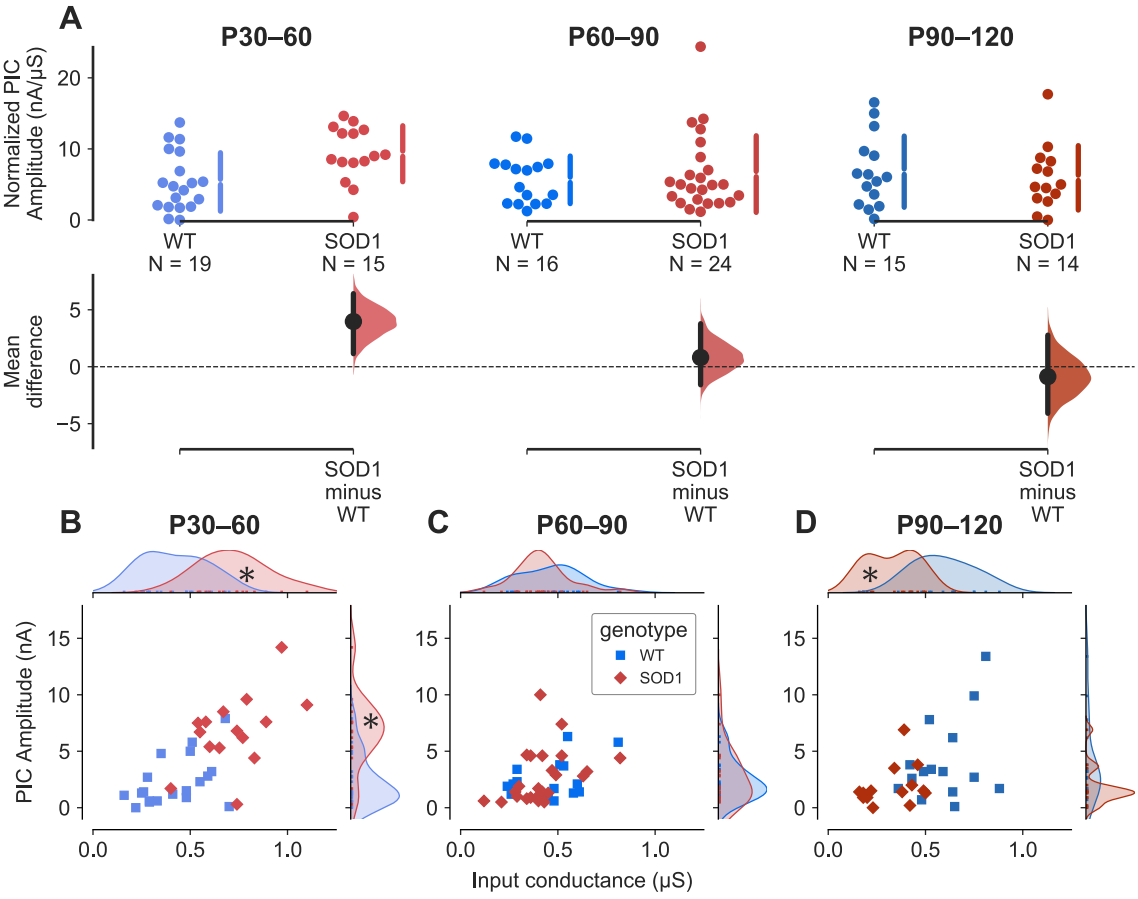
A
P30–60
P60–90
P90–120
Normalized PIC Amplitude (nA/μS)
20
10
0
WT
N = 19
SOD1
N = 15
WT
N = 16
SOD1
N = 24
WT
N = 15
SOD1
N = 14
Mean difference
5
0
−5
SOD1 minus WT
SOD1 minus WT
SOD1 minus WT
B
P30–60
C
P60–90
D
P90–120
*
*
PIC Amplitude (nA)
15
10
5
0
genotype
WT
SOD1
0.0
0.5
1.0
Input conductance (μS)

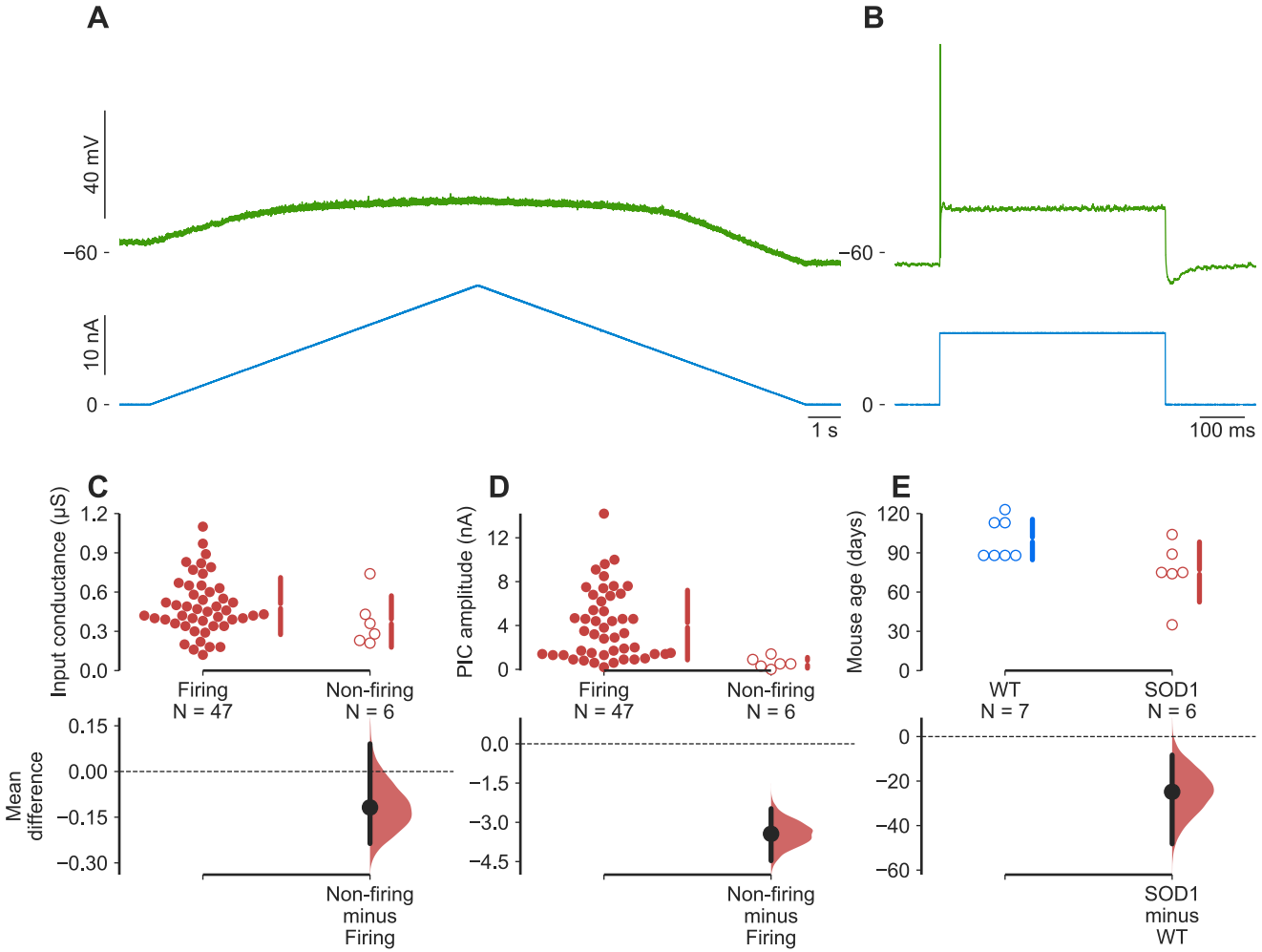
A
40 mV
−60
10 nA
0
1 s
B
−60
0
100 ms
C
Input conductance (µS)
1.2
0.9
0.6
0.3
0.0
Firing
N = 47
Non-firing
N = 6
Mean difference
0.15
0.00
−0.15
−0.30
Non-firing minus Firing
D
PIC amplitude (nA)
12
8
4
0
Firing
N = 47
Non-firing
N = 6
0.0
−1.5
−3.0
−4.5
Non-firing minus Firing
E
Mouse age (days)
120
90
60
30
0
WT
N = 7
SOD1
N = 6
0
−20
−40
−60
SOD1 minus WT

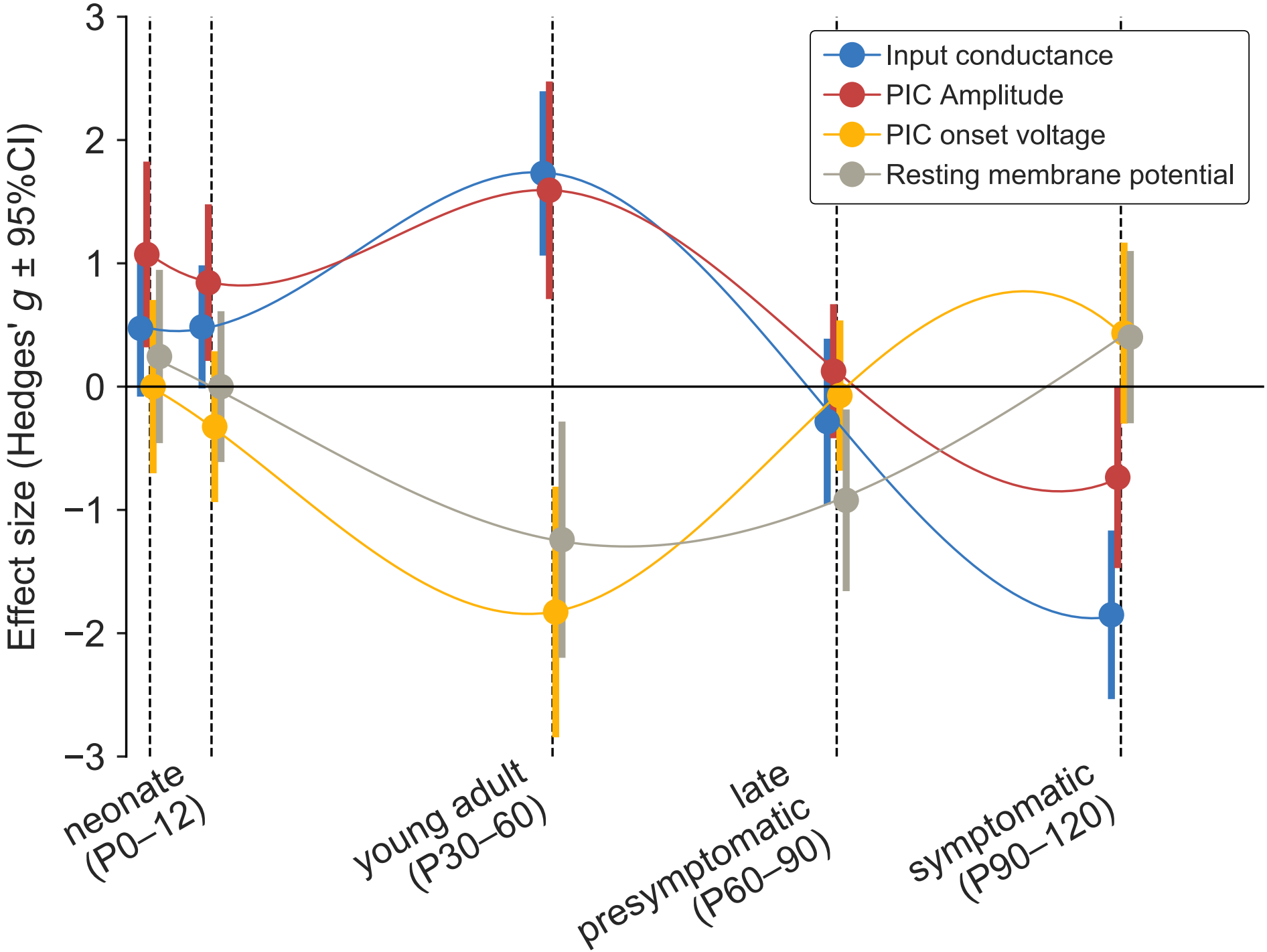
Effect size (Hedges' g ± 95%CI)
3
2
1
0
−1
−2
−3
Input conductance
PIC Amplitude
PIC onset voltage
Resting membrane potential
neonate (P0–12)
young adult (P30–60)
late presymptomatic (P60–90)
symptomatic (P90–120)

	P30–60				P60–90				P90–120			
	WT (N=19)	SOD1 (N=15)	Mean diff.	Hedges' g	WT (N=16)	SOD1 (N=24)	Mean diff.	Hedges' g	WT (N=15)	SOD1 (N=14)	Mean diff.	Hedges' g
Input conductance	0.42 ± 0.16 µS [0.35–0.49]	0.72 ± 0.18 µS [0.64–0.81]	0.30 µS [0.19—0.42] (p=2.2e−05)		0.46 ± 0.16 µS [0.39–0.54]	0.42 ± 0.15 µS [0.36–0.48]	−0.04 µS [−0.14—0.05] (p=0.39)		0.60 ± 0.15 µS [0.52–0.67]	0.33 ± 0.13 µS [0.26–0.39]	−0.27 µS [−0.37—−0.17] (p=2.1e−05)	
PIC amplitude	2.30 ± 2.17 nA [1.53–3.49]	6.73 ± 3.28 nA [5.25–8.41]	4.43 nA [2.56—6.29] (p=0.00016)		2.47 ± 1.69 nA [1.81–3.44]	2.75 ± 2.40 nA [1.99–3.89]	0.27 nA [−0.93—1.53] (p=0.67)		4.12 ± 3.69 nA [2.68–6.55]	1.90 ± 1.78 nA [1.24–3.19]	−2.22 nA [−4.63—−0.41] (p=0.05)	
Normalized PIC amplitude	5.35 ± 4.11 nA/µS [3.70–7.25]	9.32 ± 3.94 nA/µS [7.14–11.00]	3.97 nA/µS [1.15—6.42] (p=0.0075)		5.65 ± 3.35 nA/µS [4.21–7.37]	6.46 ± 5.39 nA/µS [4.81–9.30]	0.81 nA/µS [−1.59—3.78] (p=0.56)		6.80 ± 5.01 nA/µS [4.58–9.62]	5.93 ± 4.53 nA/µS [4.12–8.82]	−0.87 nA/µS [−4.09—2.77] (p=0.63)	
PIC amplitude (down ramp)	2.65 ± 2.60 nA [1.76–4.19]	5.55 ± 3.48 nA [4.07–7.46]	2.90 nA [0.86—4.89] (p=0.013)		2.29 ± 2.30 nA [1.51–3.88]	2.87 ± 2.22 nA [2.13–3.89]	0.58 nA [−1.03—1.76] (p=0.44)		4.43 ± 3.10 nA [3.06–6.07]	2.25 ± 1.98 nA [1.45–3.53]	−2.18 nA [−3.99—−0.34] (p=0.032)	
Current at transition SPR/PR	5.93 ± 3.24 nA [4.34–8.58]	8.01 ± 2.67 nA [6.50–9.22]	2.08 nA [−0.95—4.08] (p=0.13)		6.28 ± 3.92 nA [4.36–10.20]	5.23 ± 3.30 nA [4.04–7.31]	−1.04 nA [−4.72—1.39] (p=0.53)		5.90 ± 2.70 nA [4.22–7.36]	2.70 ± 2.34 nA [1.25–3.73]	−3.20 nA [−5.24—−1.28] (p=0.0081)	
Recruitment current	4.73 ± 3.14 nA [3.47–6.25]	6.21 ± 2.51 nA [4.70–7.26]	1.49 nA [−0.65—3.22] (p=0.14)		5.28 ± 2.64 nA [4.19–6.83]	4.53 ± 3.38 nA [3.33–6.23]	−0.76 nA [−2.57—1.27] (p=0.46)		5.43 ± 3.07 nA [4.05–7.10]	2.19 ± 1.56 nA [1.59–3.37]	−3.24 nA [−4.98—−1.63] (p=0.0017)	
Current at derecruitment	5.92 ± 3.76 nA [4.40–7.64]	7.64 ± 3.31 nA [5.94–9.25]	1.72 nA [−0.73—3.94] (p=0.17)		6.54 ± 4.07 nA [4.67–9.03]	5.01 ± 4.05 nA [3.54–7.11]	−1.53 nA [−4.41—1.18] (p=0.31)		5.64 ± 2.95 nA [4.04–7.18]	2.59 ± 1.58 nA [1.96–3.76]	−3.05 nA [−4.75—−1.24] (p=0.0056)	
Frequency at transition SPR/PR	54.30 ± 17.35 Hz [44.94–65.17]	57.90 ± 17.06 Hz [49.59–67.04]	3.60 Hz [−10.88—15.87] (p=0.62)		53.55 ± 13.32 Hz [44.54–61.59]	43.75 ± 13.55 Hz [36.61–49.59]	−9.79 Hz [−20.63—0.31] (p=0.11)		51.58 ± 15.41 Hz [43.14–61.44]	42.44 ± 11.34 Hz [37.05–48.95]	−9.14 Hz [−19.10—1.70] (p=0.13)	
Normalized PIC amplitude (down ramp)	6.72 ± 5.77 nA/µS [4.46–9.52]	7.85 ± 4.85 nA/µS [5.41–10.48]	1.13 nA/µS [−2.42—4.63] (p=0.56)		5.05 ± 4.43 nA/µS [3.36–7.81]	6.81 ± 5.14 nA/µS [5.13–9.32]	1.75 nA/µS [−1.16—4.57] (p=0.26)		7.77 ± 5.24 nA/µS [5.47–10.47]	6.72 ± 4.91 nA/µS [4.71–9.74]	−1.05 nA/µS [−4.38—2.82] (p=0.58)	
ΔI	1.20 ± 1.20 nA [0.70–1.74]	1.45 ± 1.25 nA [0.91–2.19]	0.25 nA [−0.54—1.10] (p=0.57)		1.47 ± 1.83 nA [0.58–2.59]	0.42 ± 1.10 nA [−0.01–0.93]	−1.04 nA [−2.22—−0.05] (p=0.093)		0.98 ± 1.32 nA [0.35–1.82]	0.39 ± 0.63 nA [0.05–0.72]	−0.58 nA [−1.50—0.13] (p=0.18)	
ΔVth	17.03 ± 6.37 mV [14.27–19.89]	18.09 ± 5.21 mV [15.06–20.40]	1.05 mV [−3.07—4.74] (p=0.61)		15.60 ± 5.54 mV [13.32–18.74]	19.26 ± 6.29 mV [16.74–22.12]	3.67 mV [−0.33—7.32] (p=0.072)		17.10 ± 5.54 mV [14.35–19.77]	13.79 ± 3.62 mV [11.99–15.78]	−3.31 mV [−6.66—0.11] (p=0.071)	
ΔF	1.79 ± 13.96 Hz [−5.45–7.06]	3.77 ± 11.06 Hz [−1.58–9.62]	1.98 Hz [−5.93—10.90] (p=0.65)		6.53 ± 17.29 Hz [0.12–22.03]	1.93 ± 8.73 Hz [−1.44–6.22]	−4.60 Hz [−19.62—2.62] (p=0.4)		−0.85 ± 7.97 Hz [−4.52–4.32]	0.75 ± 7.97 Hz [−3.93–4.43]	1.60 Hz [−5.07—7.19] (p=0.62)	
ΔVpeak	18.32 ± 7.08 mV [15.32–21.61]	19.13 ± 8.15 mV [14.12–22.39]	0.81 mV [−4.99—5.20] (p=0.76)		18.09 ± 7.71 mV [14.96–22.49]	21.18 ± 5.82 mV [19.09–23.83]	3.09 mV [−1.76—6.94] (p=0.19)		16.37 ± 8.32 mV [12.35–20.36]	15.60 ± 5.86 mV [12.48–18.68]	−0.77 mV [−6.08—4.36] (p=0.78)	
PIC end voltage	−58.67 ± 6.87 mV [−61.58—−55.73]	−61.87 ± 37.36 mV [−72.39—−24.29]	−3.20 mV [−14.21—35.70] (p=0.75)		−60.48 ± 4.90 mV [−63.38—−58.61]	−61.80 ± 7.27 mV [−64.68—−58.93]	−1.32 mV [−4.61—2.66] (p=0.5)		−65.00 ± 5.70 mV [−67.75—−62.22]	−61.30 ± 8.12 mV [−65.53—−57.16]	3.70 mV [−1.44—8.54] (p=0.17)	
F-I gain (PR, descending ramp)	19.21 ± 10.07 Hz/nA [14.81–26.71]	17.23 ± 5.15 Hz/nA [14.92–20.10]	−1.98 Hz/nA [−12.04—2.61] (p=0.58)		33.93 ± 35.75 Hz/nA [18.15–74.00]	15.25 ± 8.95 Hz/nA [11.95–21.32]	−18.68 Hz/nA [−59.63—−2.66] (p=0.22)		15.15 ± 7.14 Hz/nA [11.70–21.05]	20.05 ± 11.30 Hz/nA [15.80–28.61]	4.90 Hz/nA [−2.37—12.22] (p=0.23)	
F-I gain (PR)	9.30 ± 3.58 Hz/nA [7.41–11.65]	8.30 ± 3.37 Hz/nA [6.49–9.83]	−1.00 Hz/nA [−3.68—1.83] (p=0.5)		12.18 ± 7.30 Hz/nA [8.72–19.26]	10.28 ± 6.43 Hz/nA [8.17–14.94]	−1.90 Hz/nA [−8.81—2.94] (p=0.54)		8.01 ± 3.16 Hz/nA [6.04–9.75]	10.84 ± 9.13 Hz/nA [7.64–18.78]	2.84 Hz/nA [−0.81—10.27] (p=0.31)	
ΔVPIC	4.36 ± 5.66 mV [1.57–6.61]	2.05 ± 5.38 mV [−1.11–4.28]	−2.31 mV [−6.23—1.00] (p=0.23)		1.76 ± 5.75 mV [−0.96–4.48]	6.12 ± 5.54 mV [3.80–8.35]	4.36 mV [0.56—7.69] (p=0.025)		1.57 ± 5.10 mV [−0.90–4.05]	0.92 ± 5.94 mV [−1.70–4.53]	−0.64 mV [−4.57—3.45] (p=0.76)	
Resting membrane potential	−62.38 ± 5.52 mV [−64.65—−59.83]	−71.45 ± 8.78 mV [−75.15—−66.18]	−9.07 mV [−13.37—−3.66] (p=0.002)		−60.98 ± 5.35 mV [−63.94—−58.67]	−66.18 ± 5.63 mV [−68.60—−64.02]	−5.20 mV [−8.47—−1.59] (p=0.0067)		−64.71 ± 7.42 mV [−68.53—−61.21]	−61.99 ± 5.43 mV [−64.42—−58.75]	2.72 mV [−1.57—7.73] (p=0.27)	
Voltage threshold for spiking	−45.35 ± 5.48 mV [−47.79—−42.97]	−54.86 ± 5.15 mV [−57.06—−51.84]	−9.51 mV [−12.79—−5.75] (p=1.9e−05)		−45.39 ± 7.04 mV [−49.02—−42.24]	−47.53 ± 5.85 mV [−49.83—−44.90]	−2.14 mV [−6.20—2.13] (p=0.34)		−47.61 ± 5.00 mV [−50.02—−45.15]	−48.20 ± 5.41 mV [−50.98—−45.33]	−0.59 mV [−4.24—2.98] (p=0.77)	
PIC peak voltage	−43.83 ± 4.79 mV [−45.73—−41.42]	−52.32 ± 4.20 mV [−54.07—−49.97]	−8.49 mV [−11.41—−5.52] (p=4.8e−06)		−42.89 ± 6.94 mV [−45.79—−39.16]	−44.88 ± 5.24 mV [−46.95—−42.92]	−1.98 mV [−6.20—1.50] (p=0.34)		−48.34 ± 5.89 mV [−50.85—−45.15]	−46.24 ± 6.27 mV [−49.64—−43.28]	2.10 mV [−2.40—6.21] (p=0.36)	
PIC onset voltage	−58.03 ± 6.35 mV [−60.76—−55.23]	−69.41 ± 5.71 mV [−71.70—−65.93]	−11.38 mV [−14.95—−7.18] (p=5.1e−06)		−59.22 ± 4.88 mV [−61.92—−57.25]	−59.66 ± 6.39 mV [−61.98—−56.99]	−0.43 mV [−3.71—3.21] (p=0.81)		−63.15 ± 6.31 mV [−66.03—−59.79]	−60.12 ± 7.25 mV [−63.95—−56.64]	3.03 mV [−1.95—7.63] (p=0.24)	
PIC peak voltage (down ramp)	−43.73 ± 4.89 mV [−45.56—−41.34]	−53.63 ± 4.90 mV [−55.72—−50.97]	−9.90 mV [−13.10—−6.60] (p=2.1e−06)		−42.49 ± 8.15 mV [−45.86—−37.91]	−42.40 ± 18.84 mV [−46.83—−27.74]	0.09 mV [−5.59—13.05] (p=0.98)		−48.14 ± 5.25 mV [−50.41—−45.18]	−45.98 ± 6.26 mV [−49.33—−43.05]	2.17 mV [−2.22—5.96] (p=0.32)	